Dissociation of HCI in water nanoclusters: An

energy decomposition analysis perspective

Alexander Zech[†] and Martin Head-Gordon*,[†],[‡]

†Kenneth S. Pitzer Center for Theoretical Chemistry, Department of Chemistry, University

of California, Berkeley, California 94720, USA

‡Chemical Sciences Division, Lawrence Berkeley National Laboratory, Berkeley, California

94720, USA

E-mail: mhg@cchem.berkeley.edu

Abstract

As known, small HCl-water nanoclusters display a particular dissociation behaviour, whereby at least four water molecules are required for the ionic dissociation of HCl. In this work, we examine how intermolecular interactions promote the ionic dissociation of such nanoclusters. To this end, a set of 45 HCl-water nanoclusters with up to four water molecules is introduced. Energy decomposition analysis based on absolutely localized molecular orbitals (ALMO-EDA) is employed in order to study the importance of frozen interaction, dispersion, polarization, and charge-transfer for the dissociation. The vertical ALMO-EDA scheme is applied to HCl-water clusters along a proton-transfer coordinate varying the amount of spectator water molecules. The corresponding ALMO-EDA results show a clear preference for the dissociated cluster only in the presence of four water molecules. Our analysis of adiabatic ALMO-EDA results reveals a push-pull mechanism for the destabilization of the HCl bond based on the synergy between forward and backward charge-transfer.

Introduction

The ionic dissociation of Brønsted acids is a fundamental reaction ubiquitous in nature. A considerable amount of literature has been published on the dissociation of hydrohalic acids examining the proton-transfer in aqueous solution, $^{1-6}$ on ice surfaces, $^{7-13}$ and in water nanodroplets. $^{14-21}$ Hydrochloric acid has received particular attention due to its role in the ozone depletion around Earth's polar regions, where dissociation occurs on the surface of polar stratospheric cloud particles. $^{7,9,22-25}$ While this process occurs at temperatures around 190 K, there is also evidence for dissociation at even lower temperatures. 12,13,26,27 For instance, Gutberlet et al. reported dissociation of $HCl(H_2O)_4$ in superfluid helium nanodroplets at 0.37 K mimicking conditions of interstellar space. 28 Such $HCl(H_2O)_n$ nanoclusters (with $n \le 4$) and other hydrohalic acid analogues have been studied by many researchers with the objective to determine the smallest cluster size at which dissociation occurs spontaneously.

Previous theoretical $^{16,29-32}$ and experimental 20,21,28 studies suggest that a minimum of four water molecules is required in order to observe a dissociation of HCl. The resulting dissociation product and global minimum among $HCl(H_2O)_4$ clusters, is termed solvent-separated ion pair (SIP or in this work referred to as S^{4d} ; see Fig. 1) and is characterized by three water molecules hydrogen-bonding to the chloride anion on one side and to the hydronium cation on the other. The mechanism of ionic dissociation in $HCl(H_2O)_4$ has often been rationalized starting from an undissociated circular cluster geometry (UD; in this work U^{4u}) and involving a contact ion pair (CIP; here C^{4d}) as an intermediate. 19,33 Aggregation-induced dissociation studies also identified another pathway involving a partial aggregate cluster geometry (PA; here P^{4u}), in which $HCl(H_2O)_3$ forms a four-membered ring with the remaining water molecule hydrogen-bonded to one of the ring water molecules. 19,21,28

The role of the local environment is crucial for dissociation and has also been explored in terms of the electric field exerted on the HCl bond.³⁴ Although a good understanding of the involved cluster configurations has been developed, there has been little discussion about the role of intermolecular forces in the dissociation. Energy decomposition analysis (EDA)

schemes are a useful tool in this regard as they yield physically interpretable components which can be associated with different classes of intermolecular forces such as electrostatics, polarization, dispersion, etc. 35 The mapping from EDA components to these intermolecular forces is however not unique leading to the co-existence of several EDA schemes, $^{36-47}$ which can be broadly characterized by their use of perturbation theory or a variational formalism. Symmetry-adapted perturbation theory $(SAPT)^{40,48,49}$ is a popular scheme belonging to the former category, while most variational EDA schemes are based on the seminal work by Kitaura and Morokuma. ³⁶ So far, there have only been few examples of EDA methods applied to HCl-water nanoclusters in the literature, for instance, Milet et al. analyzed two- and threebody interactions in $HCl(H_2O)_4$ and $HCl(H_2O)_5$ clusters by means of symmetry-adapted perturbation theory (SAPT) for which they found electrostatic and induction interactions to be dominant. ³³ Similarly, Arillo Flores et al. discuss polarization and charge-transfer in the solvent structure around $\mathrm{H_3O^+}$ and $\mathrm{Cl^-}$, respectively, based on Mulliken charges. 50 Using effective two-body interactions, we recently investigated the influence of the spectator water molecules $(H_2O)_3$ on the proton-transfer subsystem $HCl \cdot H_2O.^{51}$ The results suggested that the proton transfer is being driven by the stabilization of the $(H_2O)_3$ hydrogen bond network rather than by the stabilization of the proton-transfer subsystem.

In this work, we examine the role of noncovalent intermolecular interactions in the dissociation of $HCl(H_2O)_n$ nanoclusters by means of energy decomposition analysis based on absolutely localized molecular orbitals (ALMO-EDA). ^{43,52,53} In the first part we introduce a set of $HCl(H_2O)_n$ clusters (n = [1..4]) and discuss their structural properties. In the subsequent sections, we explore ALMO-EDA components along a proton-transfer coordinate and employ the adiabatic ALMO-EDA scheme to investigate geometric effects.

ALMO-EDA

The following paragraphs comprise a brief description of the ALMO-EDA scheme. A detailed account of the derivation and definition of components is given elsewhere. $^{43,52-55}$ A general review is also available. 56 The binding energy of fragments, $\Delta E_{\rm bind}$, consists of the purely electronic interaction energy, $\Delta E_{\rm int}$, and the energy needed to deform the isolated fragments to the geometry they adopt in the complex, $\Delta E_{\rm gd}$. In its original formulation, 43 the ALMO-EDA scheme partitions the interaction energy $\Delta E_{\rm int}$ into components associated with frozen interaction (frz), polarization (pol), and charge-transfer (ct):

$$\Delta E_{\rm int} = \Delta E_{\rm frz} + \Delta E_{\rm pol} + \Delta E_{\rm ct},\tag{1}$$

The frozen term corresponds to the energy change due to assembling the complex from infinitely separated fragments without allowing a relaxation of the fragment wavefunctions. At the polarized level the constraint on the MOs is partially lifted and each fragments' MOs are allowed to relax in the field of all other fragments without exchanging electrons between them. The charge-transfer term is then defined as the energy difference between the polarized and fully relaxed total energy. For ALMO-EDA at the DFT level of theory, the frozen interaction is further decomposed ^{43,55} into contributions deriving from permanent electrostatics (elec), Pauli repulsion (pauli), and dispersion (disp):

$$\Delta E_{\rm frz} = \Delta E_{\rm elec} + \Delta E_{\rm pauli} + \Delta E_{\rm disp}.$$
 (2)

The initial ALMO-EDA scheme employed the full atomic orbital (AO) space of each fragment leading to a charge-transfer contamination of the polarized term for nearly complete basis sets. The second generation ALMO-EDA scheme provides a well-defined basis set limit for polarization and charge-transfer contributions through the use of fragment electricfield response functions (FERF). These functions define a polarization subspace inherent to each fragment, which only contains the virtual functions necessary to describe a fragment's response to weak electric fields.⁵⁷ The decomposition of the interaction energy described above occurs at a given molecular geometry and is - in analogy to electronic excitations - often referred to as *vertical* EDA. Since each intermediate level of the ALMO-EDA scheme has a corresponding, properly antisymmetrized wavefunction, it is possible to determine a molecular geometry corresponding to the minimal frozen $E_{\rm frz}^*$ or polarized total energy $E_{\rm pol}^*$. This scheme, known as *adiabatic* EDA,⁵⁸ thus incorporates geometric effects to the EDA components and yields a decomposition of the binding energy:

$$\Delta E_{\text{bind}} = (E_{\text{frz}}^* - \sum_{I}^{\text{frag}} E_I^*) + (E_{\text{pol}}^* - E_{\text{frz}}^*) + (E_{\text{tot}}^* - E_{\text{pol}}^*)$$
 (3)

$$= \Delta E_{\rm frz}^{\rm (ad)} + \Delta E_{\rm pol}^{\rm (ad)} + \Delta E_{\rm ct}^{\rm (ad)}. \tag{4}$$

The adiabatic EDA scheme has proven to be an indispensable tool to study the effect of the ALMO constraints on molecular properties. ^{59,60}

Computational Methods

All *ab initio* electronic structure calculations were performed with the Q-Chem 5.4 software package. 61 and, unless stated otherwise, the def2-TZVPD 62,63 basis set was used. All ALMO-EDA calculations (vertical and adiabatic) were performed with the ω B97M-V 64 functional, which has been found to be very accurate for intermolecular interaction energies. 65 The adiabatic ALMO-EDA results were obtained with the original ALMO-EDA approach which uses the full AO space for each fragment, as analytical gradients of the self-consistent field method for molecular interactions (SCFMI) involving FERFs are not available yet. In principal, several fragment references can be envisioned for the EDA calculations (see Supporting Information for overview). For $HCl(H_2O)_4$, a 6-fragment ionic reference was chosen to study the proton-transfer with vertical ALMO-EDA, whereas a neutral 5-fragment and 2-fragment

reference, respectively, was used with adiabatic EDA. All DFT calculations based on the ω B97M-V functional used the SG-2 standard grid ⁶⁶ for the numerical integration of the exchange-correlation functional and the SG-1 standard grid ⁶⁷ for the non-local correlation component, respectively. Numerical integrations pertaining to the BLYP, ^{68,69} HFLYP, ^{69,70} BHHLYP, 68,69,71 CAM-B3LYP 72 and B3LYP 71,73 functionals were performed with the SG-2 standard grid. Single-point calculations based on second order Møller-Plesset perturbation theory (MP2) employed resolution of the identity in conjunction with the aug-cc-pVTZ⁷⁴ auxiliary basis set. Additionally, core orbitals were not included for the evaluation of the correlation energy (frozen core approximation). Geometry optimizations (including adiabatic EDA) were considered converged if the maximum gradient component was smaller than $1.5 \cdot 10^{-4}$ a.u. and the energy change between cycles less than $7.5 \cdot 10^{-7}$ Hartree. The conformational space of $HCl(H_2O)_n$ (n = [1..4]) was explored using the tight-binding method GFN2-xTB⁷⁵ together with the Conformer–Rotamer Ensemble Sampling Tool (CREST).⁷⁶ Each molecular geometry obtained in this fashion was subsequently optimized at $\omega B97M$ -V/def2-TZVPD level of theory and verified to describe a stationary point by computing harmonic vibrational frequencies. A cluster geometry was discarded from the set if it showed an imaginary frequency or if it compared to an accepted structure with a root-mean-square deviation of less than 0.1 Å.

Cluster Conformers

Employing the conformational sampling described above and subsequent optimization at the DFT level we obtained 45 different $HCl(H_2O)_n$ cluster geometries (n = [1..4]), of which 10 exhibit a dissociated HCl molecule. The structures obtained in this fashion are in a good agreement with geometries reported in the literature. ^{29–31,34,77} Figure 1 presents an overview of selected cluster geometries arranged by the number of water molecules (a depiction of all optimized structures is presented in the Supporting Information). In the following, we will

refer to these structures by a label comprised of a letter indicating the cluster topology (e.g. \mathbf{U} , see text below), a superscript containing the number of water molecules (n) followed by a letter indicating a dissociated (d) or undissociated (u) cluster, and a subscript corresponding to the index of the cluster within each group (sorted by total electronic energy). Cluster geometries for which the assignment is ambiguous will use the letter X instead. Most of the clusters presented in Figure S1 can be grouped according to several reoccurring structural motifs. Often the most favoured undissociated cluster (U) exhibits circular and nearly planar arrangement, whereby every fragment acts as a hydrogen-bond donor and acceptor (cf. U_1^{2u} , ${f U}_1^{3{f u}}$ and ${f U}_{14}^{4{f u}}).$ The partial aggregate $({f P})$ cluster is characterized by the HCl molecule forming a ring with n-1 water molecules while the nth water is hydrogen-bonded to the ring (e.g. \mathbf{P}_{22}^{4u}). In the aggregate (A) type of cluster, on the other hand, all n water molecules form a ring-like structure with the HCl attached laterally (e.g. A_8^{4u}). The more unfavourable isomers contain strained H-bonds or smaller rings (or both), such as X_{29}^{4u} , whereby one H_2O acts as a double hydrogen-bond donor and acceptor forming two 3-fragment rings arranged perpendicular to each other. The most favoured dissociated cluster, the solvent-separated ion pair (S) (\mathbf{S}_1^{4d} and \mathbf{S}_2^{4d}), comprises an Eigen cation ^{78–80} ($\mathbf{H}_3\mathbf{O}^+(\mathbf{H}_2\mathbf{O})_3$), i.e. the chloride and hydronium ions are coupled only indirectly via three water molecules. The contact ion pair (\mathbf{C}) is characterized by hydrogen-bonding between $\mathrm{H_3O^+}$ and Cl^- , with the remaining water molecules forming hydrogen-bonds to the two ions and among each other (e.g. C_3^{4d}).

Figure 2 shows the HCl bond length of the cluster geometries considered in this work (for dissociated species the distance between chloride and closest hydrogen atom is considered). Sorted by HCl bond length, three distinct zones emerge corresponding to undissociated clusters (1.3 to 1.4 Å), contact ion pairs (1.7 to 1.9 Å) and solvent-separated ion pairs (ca. 2.1 Å). Interestingly, two cluster geometries, \mathbf{U}_3^{2u} and \mathbf{X}_4^{2u} , exhibit a shorter r(HCl) bond length than the monohydrate $\text{HCl} \cdot \text{H}_2\text{O}$. This is most likely due to one of the water molecules acting as a double H-bond acceptor leading to a less favourable $\text{ClH} \cdots \text{OH}_2$ hydrogen bonding interaction. For n=3, we obtain a structure (\mathbf{X}_4^{3u}) which contains the second longest

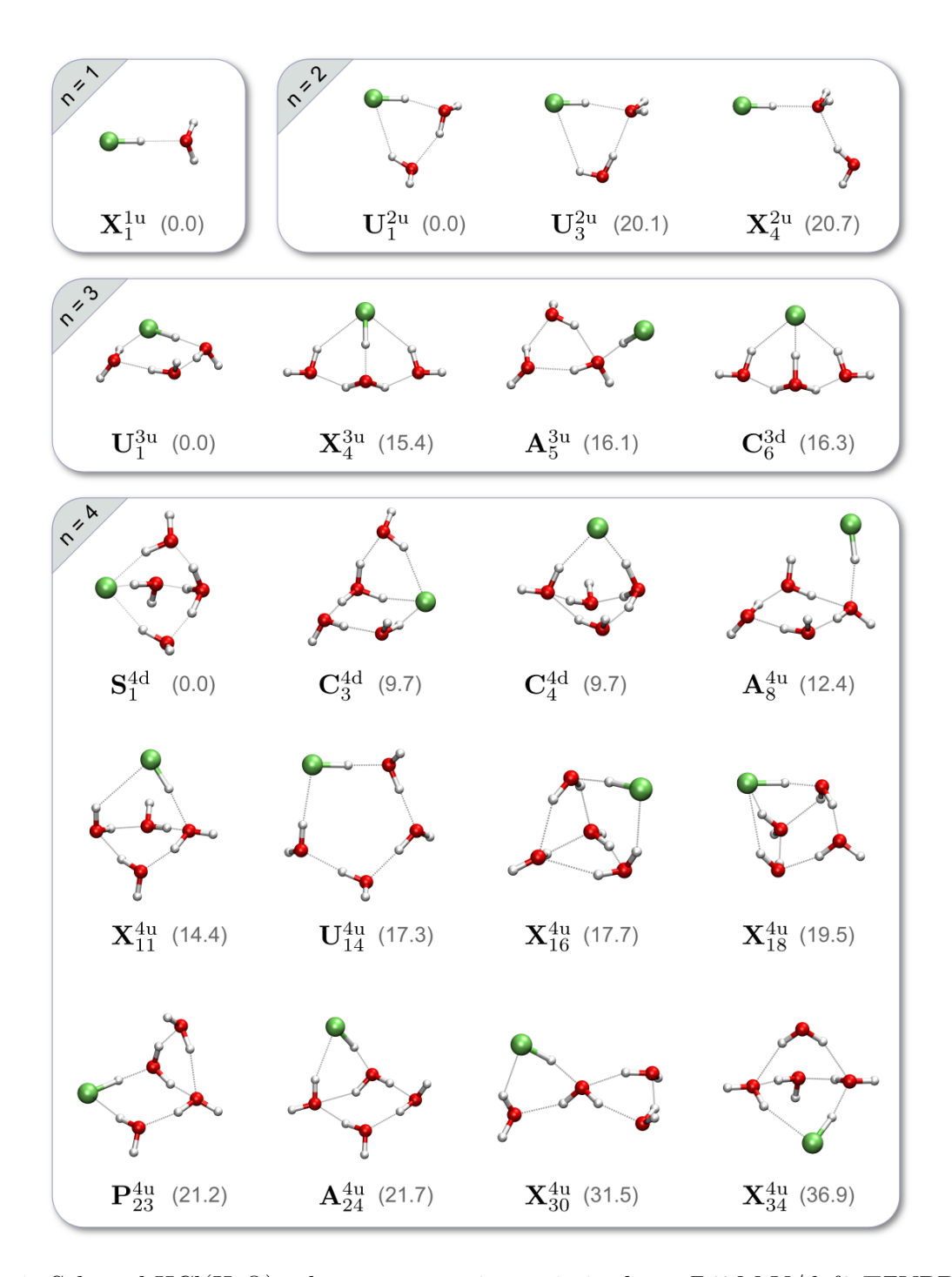


Figure 1: Selected $HCl(H_2O)_n$ cluster geometries optimized at $\omega B97M\text{-V/def2-TZVPD}$ level of theory sorted by number of water molecules. The label indicates the cluster motifs, such as undissociated ring (**U**), aggregate (**A**), partial aggregate (**P**), solvent-separated ion pair (**S**), contact ion pair (**C**), and uncategorized (**X**). Additionally, the relative electronic energy (in kJ/mol) within each group is shown in parentheses. $HCl(H_2O)_4$ in particular gives rise to a multitude of different cluster motifs.

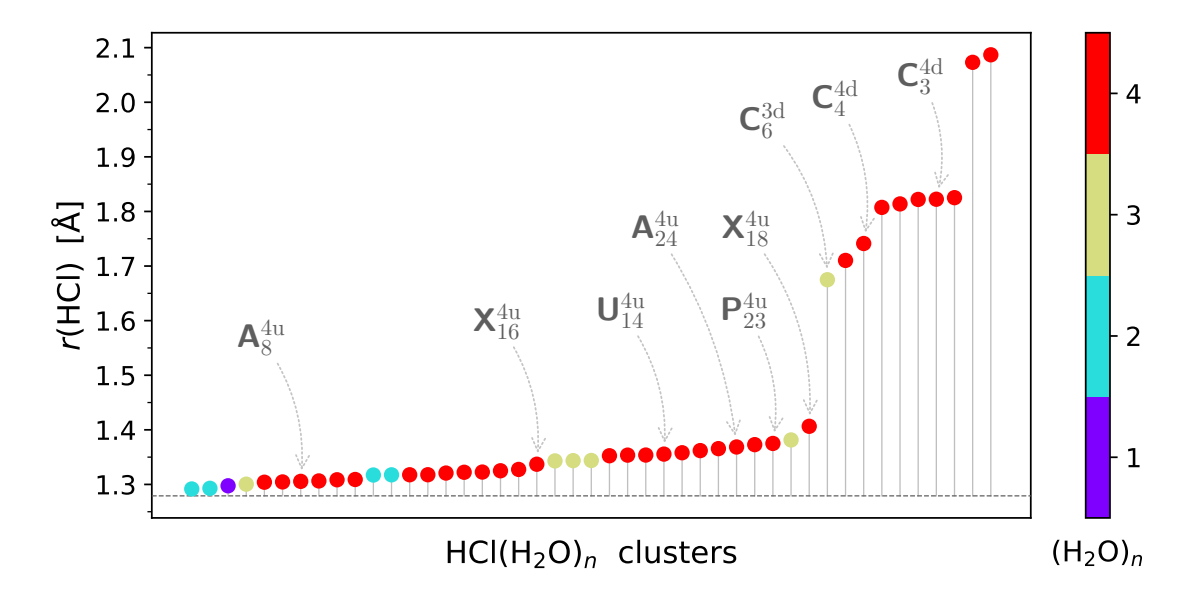


Figure 2: Distance (in Ångstrøm) between chlorine atom and closest hydrogen atom for all conformers in this study. The dashed horizontal line marks the HCl bond length in the optimized gas-phase structure. The colors indicate the number of water molecules (including hydronium ion) in each cluster. Selected clusters as presented in Fig. 1 are labelled explicitly. Three distinct zones of HCl distances emerge, corresponding to undissociated, contact ion pair and solvent-separated ion pair.

HCl bond length $(r(\text{HCl}) = 1.381\,\text{Å})$ among all undissociated cluster geometries. The set presented herein also contains this cluster in its dissociated form (\mathbf{C}_6^{3d}) , whereby the barrier in electronic energy from \mathbf{C}_6^{3d} to \mathbf{X}_4^{3u} is extremely small $(0.3\,\text{kJ/mol})$ (see Figure S3). Re-optimization with CAM-B3LYP, BHHLYP and HFLYP (each using the def2-TZVPD basis set) also predicts a dissociated cluster, whereas re-optimization at BLYP/def2-TZVPD, B3LYP/def2-TZVPD and RIMP2/aug-cc-pVTZ levels of theory reverts back to the undissociated species (\mathbf{X}_4^{3u}) . Previous studies have reported this cluster both in its dissociated and undissociated 17,31,34,77,81 form suggesting that the existence of \mathbf{C}_6^{3d} is very sensitive to the chosen computational model.

Among undissociated $HCl(H_2O)_4$ clusters, the longest HCl bond length is found for \mathbf{X}_{18}^{4u} with $r(HCl) = 1.406\,\text{Å}$. With the proton nearly at the geometric center of Cl and O, this structure can in fact be seen as a limit case of an undissociated cluster whereby HCl is on the brink of dissociation. Since we observed a strong dependence in \mathbf{C}_6^{3d} on the chosen

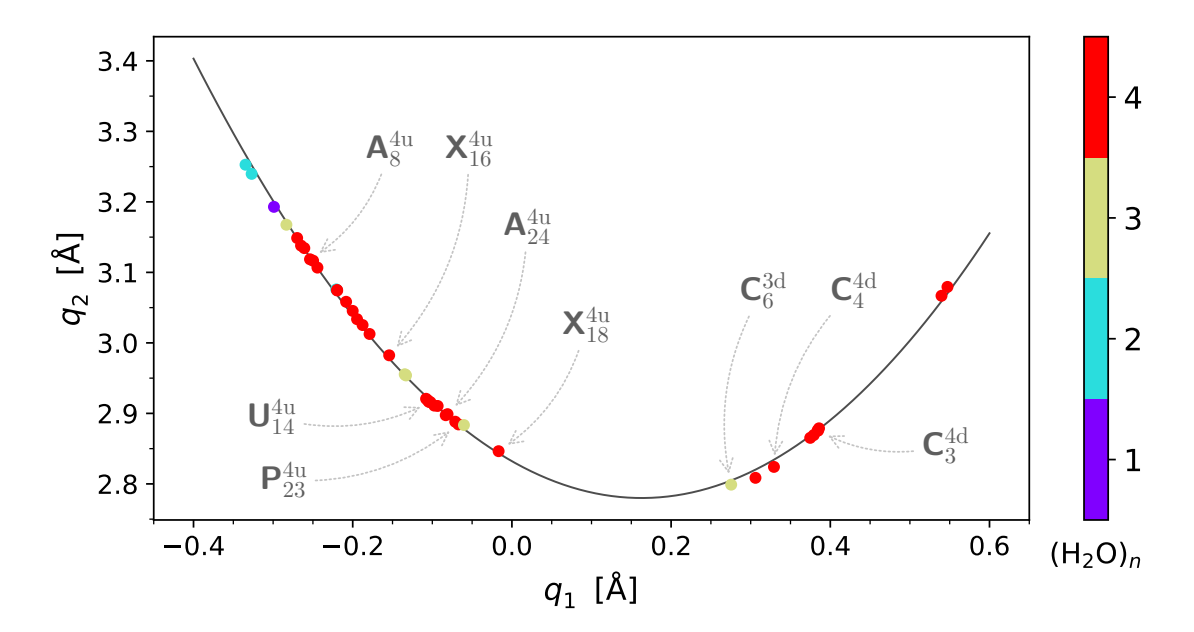


Figure 3: Correlation between $q_1 = \frac{1}{2} \left(r(\text{HCl}) - r(\text{OH}) \right)$ and $q_2 = r(\text{HCl}) + r(\text{OH})$. The solid line was obtained from a least-squares quadratic fit yielding $f(q_1) = 1.966 \, q_1^2 - 0.641 \, q_1 + 2.832$. The colors indicate the number of water molecules (including H_3O^+) in each cluster. Selected clusters as presented in Fig. 1 are labelled explicitly. A grouping of $HCl(H_2O)_n$ nanoclusters occurs which show a similar q_1 - q_2 -relationship.

functional approximation, $\mathbf{X}_{18}^{4\mathrm{u}}$ was also optimized at the MP2/aug-cc-pVTZ level of theory, which resulted in a similarly stretched HCl bond ($r(\mathrm{HCl}) = 1.413\,\mathrm{\mathring{A}}$).

Another way to illustrate the degree of proton transfer is by considering the quadratic relation between the displacement of the proton from the Cl-O midpoint $(q_1 = \frac{1}{2} (r(\text{HCl}) - r(\text{OH})))$ and the Cl-O distance $(q_2 = r(\text{HCl}) + r(\text{OH}))$. 32,82,83 Large negative values of q_1 indicate an undissociated HCl molecule, whereas large positive values indicate the presence of H_3O^+ and Cl^- . For $q_1 = 0$ the proton is located at the geometric center between Cl and O. The resulting plot of the q_1 - q_2 relation is presented in Figure 3. Apart from the limit case of \mathbf{X}_{18}^{4u} discussed above, there appears a clustering of points for $q_1 \approx -0.1$, all of which correspond to either a P- or U-type geometry.

From a structural analysis of coordination motifs of HCl, it seems that a prerequisite for HCl bond length elongation (and therefore dissociation) is two-fold. Firstly, the water molecule to which the proton is transferred adopts a double donor structure as noted in Ref. 34. Examples for this motif are $\mathbf{U}_{21}^{4\mathrm{u}}$ and $\mathbf{P}_{23}^{4\mathrm{u}}$, which contain the third and fourth longest HCl bond lengths in undissociated clusters, respectively. Secondly, the chlorine atom acts also as a double hydrogen acceptor to two nearby water molecules as observed in clusters $\mathbf{X}_{4}^{3\mathrm{u}}$ and $\mathbf{X}_{18}^{4\mathrm{u}}$.

Dissociation

The aim of the following section is to analyze the individual EDA components along a dissociation coordinate. To this end, we employ a fragment reference involving a proton fragment, i.e. $(H^+)(Cl^-)(H_2O)_4$, for all ALMO-EDA calculations, such that HCl and H_3O^+ are treated on equal footing along the proton-transfer coordinate. Two cluster geometries of undissociated HCl, \mathbf{X}_{18}^{4u} and \mathbf{P}_{23}^{4u} , were chosen as starting points for a dissociation coordinate (results based on \mathbf{P}_{23}^{4u} are collected in the Supporting Information). As the stretched HCl bond is close to dissociation and requires little reorganization of the cluster geometry, the $O1\cdots H1$ distance is a good approximation for a proton-transfer coordinate. Analogous to the previous section the proton-transfer coordinate was created by performing a relaxed scan for fixed values of the $O1\cdots H1$ distance ranging from 0.9 to 2.5 Å (see Figure 4). The resulting PES shows that the equilibrium structure of \mathbf{X}_{18}^{4u} corresponds to a shallow minimum. Following along this coordinate towards dissociation of HCl, a very small barrier (< 0.5 kJ/mol) appears, after which the energetically more favourable dissociated cluster \mathbf{C}_{10}^{4d} is obtained (see Supporting Information).

To assess the role of the water cluster in the dissociation, additional ALMO-EDA calculations were performed by incrementally adding spectator water molecules (W2, W3, W4) starting from the (H⁺)(Cl⁻)(W1) subsystem. We would like to point out that the incrementally constructed cluster geometries are subsets of the full cluster geometry and no re-optimization was performed.

Figure 5 shows the interaction energy along the dissociation coordinate for fully and par-

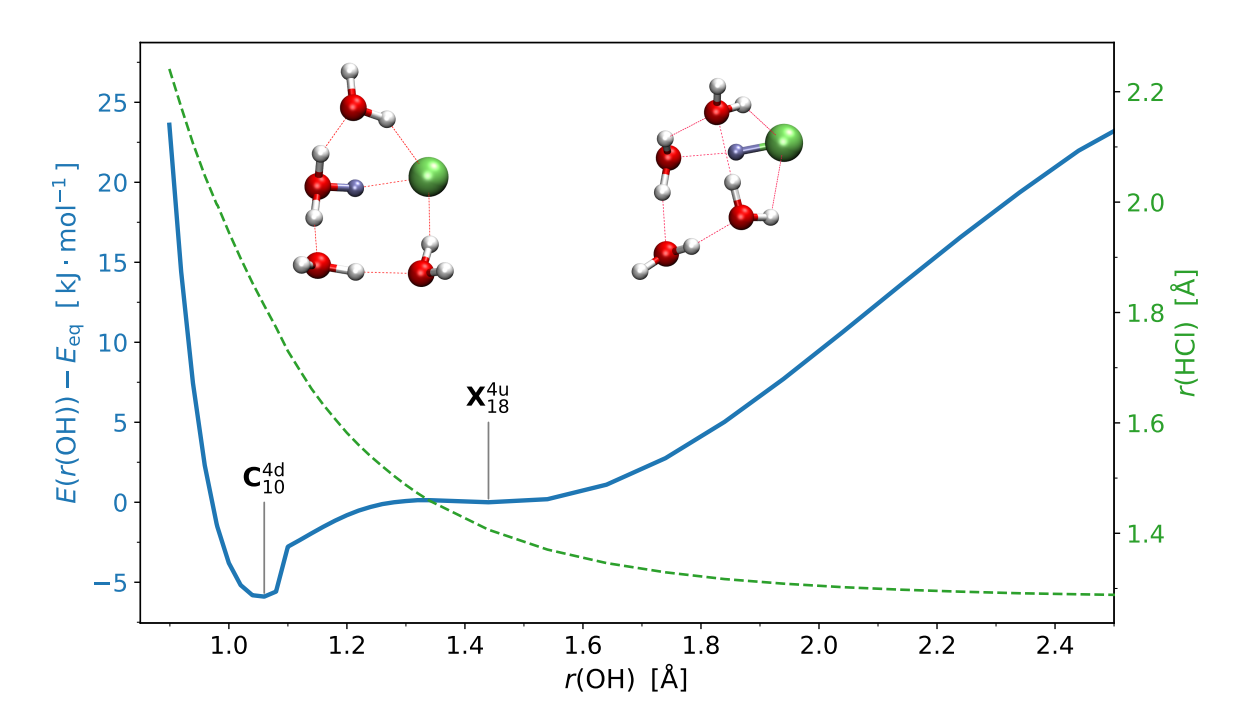


Figure 4: Relaxed potential energy surface scan of $\mathbf{X}_{18}^{4\mathrm{u}}$ along the proton transfer coordinate r_{OH} (level of theory: $\omega \mathrm{B97M\text{-}V/def2\text{-}TZVPD}$). The energy (blue) is given in kJ/mol relative to the equilibrium geometry of $\mathbf{X}_{18}^{4\mathrm{u}}$ (E_{eq}), whereas the H-Cl distance is shown in Å (green). Additionally, the HCl-water clusters $\mathbf{C}_{10}^{4\mathrm{d}}$ (left) and $\mathbf{X}_{18}^{4\mathrm{u}}$ (right) are displayed with the transferred proton highlighted in dark blue. Starting from the undissociated species, the proton-transfer occurs almost barrierlessly.

tially solvated \mathbf{X}_{18}^{4u} . Due to defining the proton as a single fragment the interaction energies are on the order of magnitude of the negative dissociation energy of HCl ($-1394\,\mathrm{kJ/mol}$). It can be seen from the graph that the incremental addition of water molecules leads to a greater stabilization in the dissociated regime ($r_{\mathrm{OH}} \approx 1.05\,\mathrm{\mathring{A}}$) as compared to the undissociated regime. As a consequence interaction energies for the dissociated and undissociated equilibrium structures become nearly equivalent once the incrementally solvated cluster contains three water molecules (orange curve in Fig. 5). With all four waters included, the interactions in the dissociated cluster (\mathbf{C}_{10}^{4d}) become more favourable ($\Delta\Delta E_{\mathrm{int}} = -20.4\,\mathrm{kJ/mol}$) as compared to the undissociated cluster (\mathbf{X}_{18}^{4u}). The contributions of each ALMO-EDA

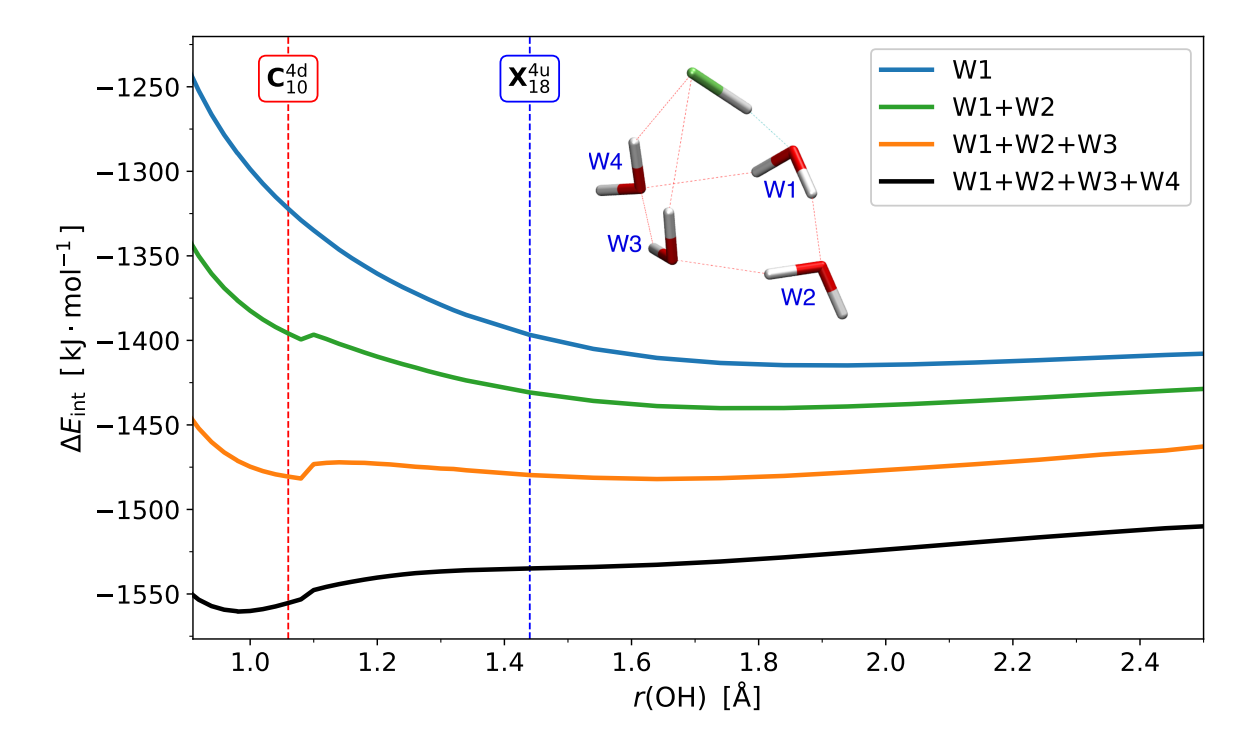


Figure 5: Interaction energy $\Delta E_{\rm int}$ of \mathbf{X}_{18}^{4u} along the dissociation coordinate defined in Fig. 4. In addition to results from the full cluster (black), the plot also shows interaction energies for partial cluster geometries using one (blue), two (green) or three (orange) water molecules. The dotted vertical lines mark the equilibrium structures of \mathbf{X}_{18}^{4u} (blue) and \mathbf{C}_{10}^{4d} (red), respectively. The incremental addition of the water molecules leads to an increasingly favourable interaction energy in the dissociated regime.

component associated with the interaction energies from Fig. 5 are presented in Figures 6-9. The frozen interaction (Fig. 6), is strongly attractive irrespective of the number of water

molecules considered as it is dominated by the strong electrostatic interaction of H⁺ and Cl⁻. The individual curves exhibit minima in the vicinity of $r_{\rm OH} = 1.2\,\rm \mathring{A}$, which correspond to the O···H separation of strongest electrostatic attraction with minimal Pauli repulsion (see also Fig. S4). Similar to the overall interaction energy, the incremental addition of water molecules has the largest effect in the dissociated regime, whereby the $\Delta E_{\rm frz}$ becomes more positive with increasing number of water molecules. This ordering of $\Delta E_{\rm frz}$ reverses in the vicinity of \mathbf{X}_{18}^{4u} , i.e. $r_{\rm OH} > 1.4\,\rm \mathring{A}$, after which $\Delta E_{\rm frz}$ is most attractive for the complete cluster (W1+W2+W3+W4). The difference in ordering between the undissociated and dissociated regime can be explained in part by the overall reduction of inter-fragment separations, which on average are 0.17 $\rm \mathring{A}$ shorter for \mathbf{C}_{10}^{4d} as compared to \mathbf{X}_{18}^{4u} , thus leading to increased Pauli repulsion. As shown in Fig. 7, the dispersive interaction varies very little

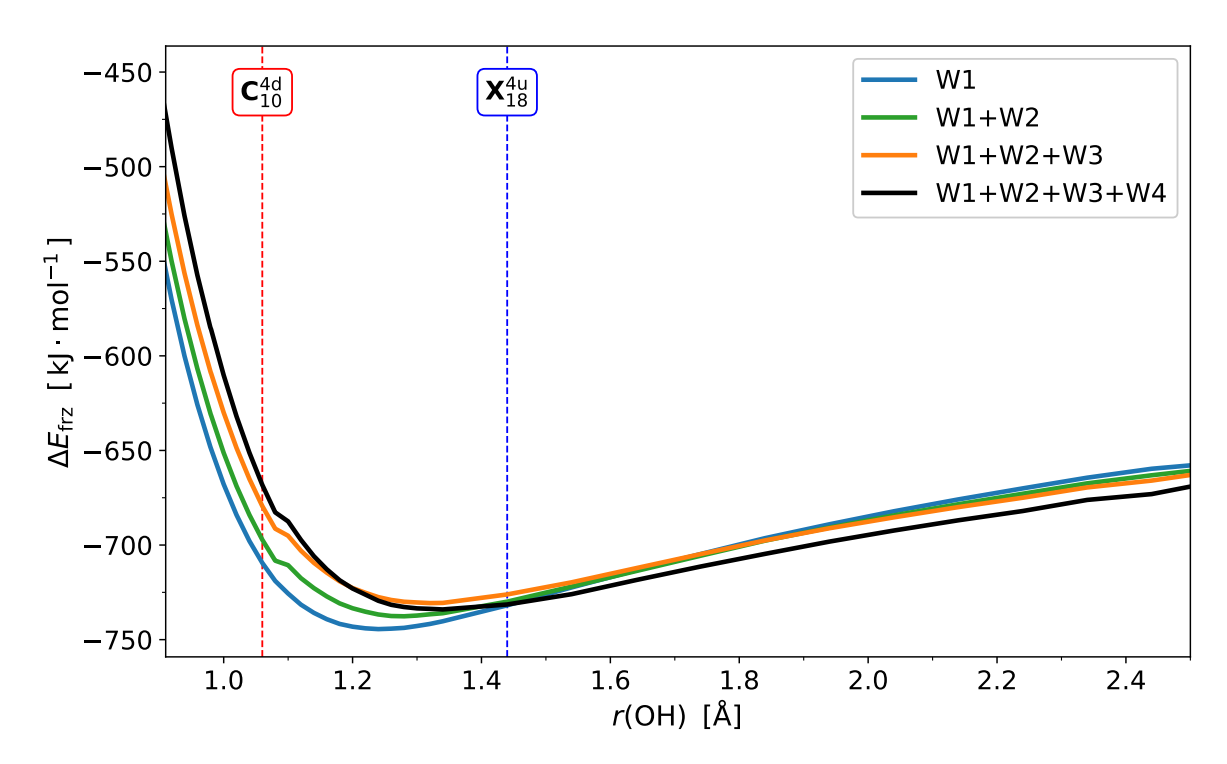


Figure 6: Frozen energy component $\Delta E_{\rm frz}$ along the dissociation coordinate of \mathbf{X}_{18}^{4u} defined in Fig. 4. In addition to results from the full cluster (black), the plot also shows energy components for partial cluster geometries using one (blue), two (green) or three (orange) water molecules. The dotted vertical lines mark the equilibrium structures of \mathbf{X}_{18}^{4u} (blue) and \mathbf{C}_{10}^{4d} (red), respectively. Overall the incremental addition of water molecules makes little difference to the magnitude of $\Delta E_{\rm frz}$.

along the considered PES coordinate. Nonetheless, $\Delta E_{\rm disp}$ becomes more attractive going from the undissociated to the dissociated regime for all but the mono-hydrate variant (W1). With step-wise solvation, each additional water molecule contributes approximately 25% of the full-cluster dispersion component. The polarization components for the incrementally

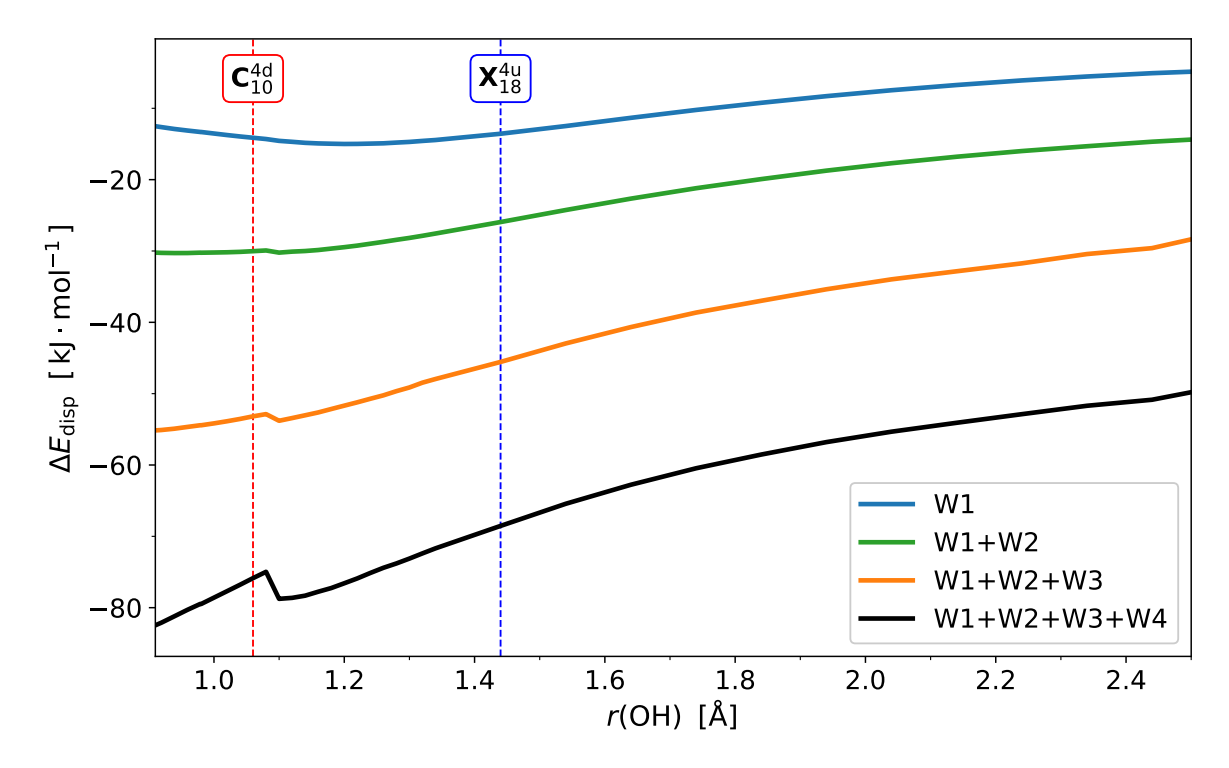


Figure 7: Dispersion component $\Delta E_{\rm disp}$ along the dissociation coordinate of \mathbf{X}_{18}^{4u} defined in Fig. 4. In addition to results from the full cluster (black), the plot also shows energy components for partial cluster geometries using one (blue), two (green) or three (orange) water molecules. The dotted vertical lines mark the equilibrium structures of \mathbf{X}_{18}^{4u} (blue) and \mathbf{C}_{10}^{4d} (red), respectively. Albeit small in magnitude, addition of water molecules leads to a large relative change of $\Delta E_{\rm disp}$.

solvated clusters are shown in Fig. 8. The general course of the polarization interaction along the coordinate is inverse to the corresponding frozen interaction, i.e. instead of a minimum $\Delta E_{\rm pol}$ displays a maximum, which can be interpreted as a point of least reorganization of fragment densities. This opposing trend of the polarization component has also been noticed as part of a SAPT-based analysis of water-halide interactions. ⁸⁴ As the water molecules are included incrementally, the maximum of $\Delta E_{\rm pol}$ moves from 1.2 Å to ca. 1.3 Å. This shift towards longer $O \cdots H$ distances may be explained by the fact that water W1 and Cl⁻ are

polarized in the same direction on the O1-H1-Cl axis, i.e. with polarization of the density of W1 towards H1 (and polarization of the density of Cl⁻ away from H1) polarization will be reduced if the proton moves in the same direction, i.e. closer to Cl⁻. Just as for $\Delta E_{\rm int}$, the incremental addition of water molecules leads to a stronger attractive interaction in the dissociated regime, e.g. the $\Delta E_{\rm pol}$ difference between the mono-hydrate cluster (W1) and the full cluster (W1+W2+W3+W4) is approximately twice as much for \mathbf{C}_{10}^{4d} in comparison to \mathbf{X}_{18}^{4u} .

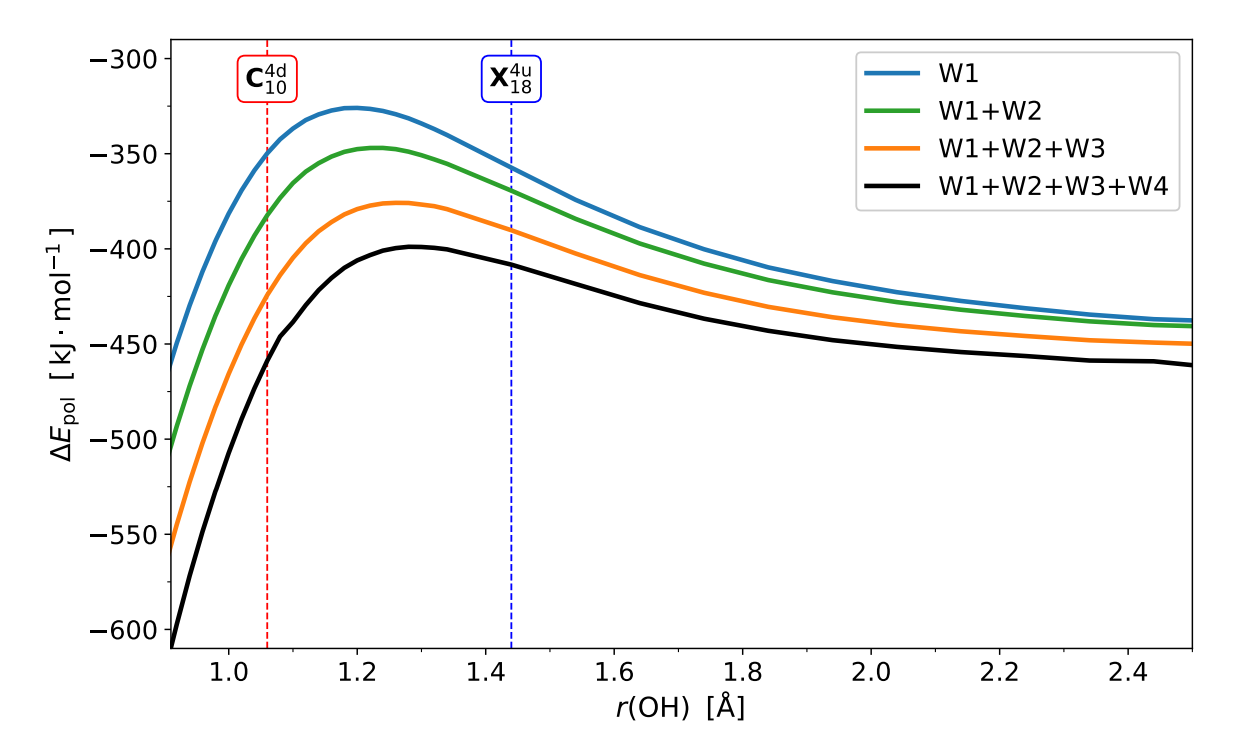


Figure 8: Polarization component $\Delta E_{\rm pol}$ along the dissociation coordinate of \mathbf{X}_{18}^{4u} defined in Fig. 4. In addition to results from the full cluster (black), the plot also shows energy components for partial cluster geometries using one (blue), two (green) or three (orange) water molecules. The dotted vertical lines mark the equilibrium structures of \mathbf{X}_{18}^{4u} (blue) and \mathbf{C}_{10}^{4d} (red), respectively. The polarization curves follow a trend inverse to $\Delta E_{\rm frz}$.

The charge-transfer term (Fig. 9) shows the largest disparity between the undissociated and dissociated regime. At short $O \cdots H$ distances, $\Delta E_{\rm ct}$ becomes more repulsive for the first two partial clusters (W1 and W1+W2), for the tri-hydrate (W1+W2+W3) it remains at about $-320\,\mathrm{kJ/mol}$, and only for the full cluster a considerable shift towards a more attractive charge-transfer energy component is observed. As a consequence, the incremental

solvation encompasses large changes. For instance, for X_{18}^{4u} the difference between monohydrate cluster (W1) and full cluster (W1+W2+W3+W4) amounts to ca. 40 kJ/mol, while it is approximately 2.5 times as much for C_{10}^{4d} . For larger separations of (H⁺)(Cl⁻) from water W1, i.e. for $r_{OH} > 1.7 \,\text{Å}$, the HCl distance changes only very little (cf. Fig. 4) and the difference between the curves mainly reflects the charge-transfer between the water molecules, which is of similar magnitude as what has been reported ⁵⁹ for the water dimer (ca. $-7.5 \,\text{kJ/mol}$) using ALMO-EDA at a comparable level of theory.

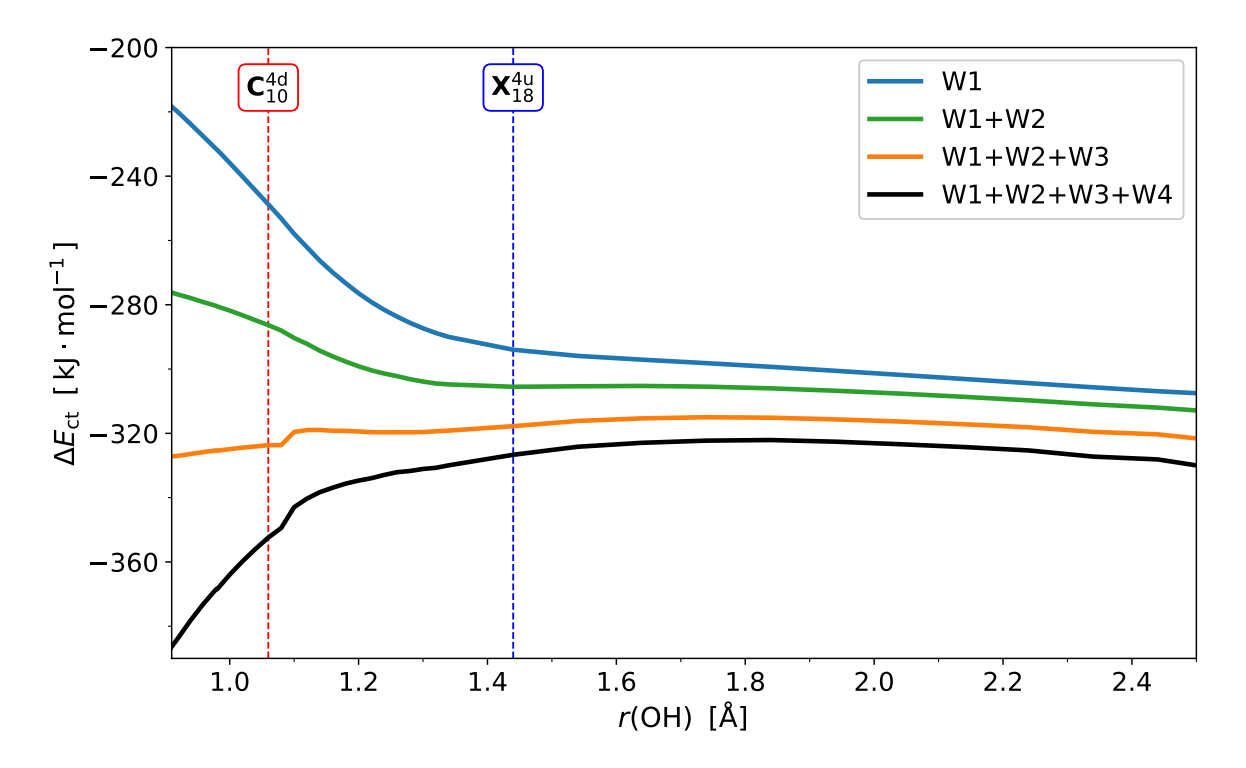


Figure 9: Charge-transfer component $\Delta E_{\rm ct}$ along the dissociation coordinate of \mathbf{X}_{18}^{4u} defined in Fig. 4. In addition to results from the full cluster (black), the plot also shows energy components for partial cluster geometries using one (blue), two (green) or three (orange) water molecules. The dotted vertical lines mark the equilibrium structures of \mathbf{X}_{18}^{4u} (blue) and \mathbf{C}_{10}^{4d} (red), respectively. The addition of water molecules strengthen the CT interaction especially in the dissociated regime, such that it reverses its trend from less favourable to more favourable.

Figure 10 compares the difference of energy components between the dissociated and undissociated regime evaluated as $\Delta \Delta E = \Delta E(\mathbf{C}_{10}^{4d}) - \Delta E(\mathbf{X}_{18}^{4u})$. The resulting terms may thus help to elucidate the lowering of the interaction energy for the full cluster observed

in Fig. 5. Starting with the frozen interaction, $\Delta\Delta E_{\rm frz}$ increases with each added water molecule, rendering the dissociated cluster progressively unfavorable in comparison to \mathbf{X}_{18}^{4u} . The relative dispersion interaction indicates a slightly more favorable interaction for \mathbf{C}_{10}^{4d} , whereby the largest stabilization occurs for the tri-hydrate (-7.63 kJ/mol). For di-hydrate and larger cluster, the difference in polarization shows a strong stabilization towards the dissociated configuration, which is growing with each additional water molecule and is of similar magnitude as $\Delta\Delta E_{\rm frz}$. Only the mono-hydrate (W1) cluster involves stabilization of the undissociated cluster \mathbf{X}_{18}^{4u} at the polarized level. Finally, the relative charge-transfer

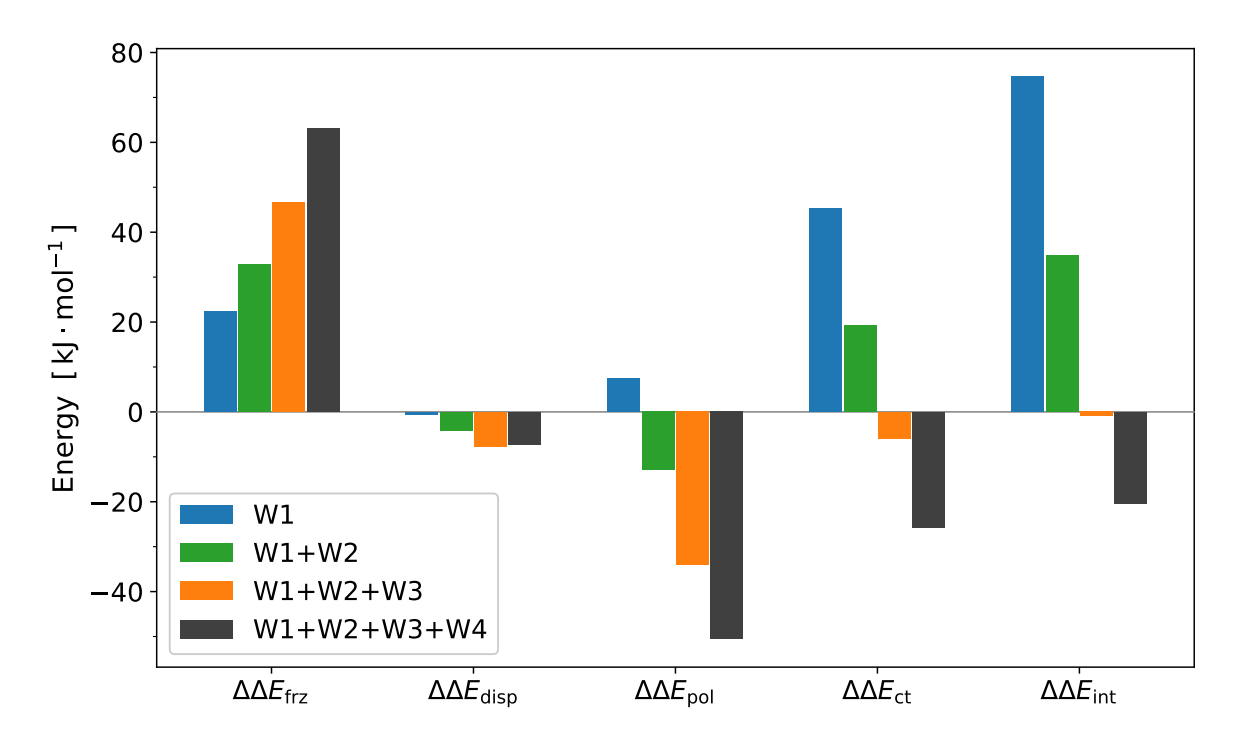


Figure 10: Difference of ALMO-EDA terms ($\Delta\Delta E = \Delta E(\mathbf{C}_{10}^{4d}) - \Delta E(\mathbf{X}_{18}^{4u})$) in the dissociated and undissociated regime. In addition to results from the full cluster (black), the plot also shows $\Delta\Delta E$ components for partial cluster geometries using one (blue), two (green) or three (orange) water molecules. A significant stabilization of \mathbf{C}_{10}^{4d} over \mathbf{X}_{18}^{4u} occurs only in the presence of all four water molecules.

interaction indicates a preference for the undissociated configuration in the presence of one (W1) or two (W1+W2) water molecules. With the inclusion of W3, $\Delta\Delta E_{\rm ct}$ changes sign, but only for the full cluster a strong stabilization for the dissociated configuration is observed (-25.76 kJ/mol). Interestingly, $\Delta\Delta E_{\rm ct}$ seems to be proportional to $\Delta\Delta E_{\rm int}$. In other words,

 $\Delta\Delta E_{\rm frz}$, $\Delta\Delta E_{\rm disp}$ and $\Delta\Delta E_{\rm pol}$ cancel each other out to a certain extent and their sum yields a net positive term, i.e. favouring the undissociated configuration. Although polarization is the most significant contribution for the relative stabilization of C_{10}^{4d} , it should also be examined in view of $\Delta\Delta E_{\rm frz}$, i.e. the strong relative stabilization (of the dissociated cluster) due to polarization emerges as a consequence of the destabilization due to the frozen interaction.

With respect to the incremental solvation, all contributions (except $\Delta\Delta E_{\rm disp}$) favour the undissociated cluster \mathbf{X}_{18}^{4u} for the case of the mono-hydrate (W1). Although the addition of the second water molecule (W2) increases stabilization for the dissociated configuration through polarization, it cannot overcome the destabilization by the frozen and charge-transfer interaction. Once the third water molecule (W3) is added, the polarization and charge-transfer interactions are significantly more stabilizing for the dissociated configuration, such that the effect of the frozen interaction is effectively canceled out. As a consequence, neither the dissociated nor the undissociated configuration is preferred. Adding the fourth water molecule enhances the propensity of polarization and charge-transfer to stabilize the dissociated configuration, which in combination with dispersion now significantly surmount the frozen interaction.

These results imply that at least three water molecules are necessary to render the charge-transfer interaction more stabilizing for the dissociated species than the corresponding neutral cluster. However, only with all four water molecules involved the relative gain in interaction energy is large enough to be significant. Thus, the relative stabilization of the interaction energy ($\Delta\Delta E_{\rm int}$) for the full cluster indicates a distinct preference for C_{10}^{4d} , which supports the minimum amount of four water molecules required for the dissociation of HCl as reported in the literature. $^{21,28,32,34,81,85-88}$

Adiabatic ALMO-EDA

Rather than analyzing the contribution of individual EDA components, it is also possible to study its direct effect on the molecular geometry by means of adiabatic ALMO-EDA. To

this end we selected 12 undissociated clusters exhibiting the strongest HCl bond elongation to be studied with adiabatic EDA, which are \mathbf{X}_{4}^{3u} , \mathbf{X}_{18}^{4u} , \mathbf{P}_{22}^{4u} , \mathbf{P}_{23}^{4u} , \mathbf{P}_{26}^{4u} , \mathbf{U}_{14}^{4u} , \mathbf{U}_{17}^{4u} , \mathbf{U}_{19}^{4u} , \mathbf{U}_{20}^{4u} , \mathbf{U}_{21}^{4u} , \mathbf{A}_{24}^{4u} . In the further course we focus on three representative clusters from this set, namely \mathbf{P}_{23}^{4u} , \mathbf{U}_{14}^{4u} , \mathbf{X}_{18}^{4u} . Starting with \mathbf{X}_{18}^{4u} , the values of selected bond lengths and bond

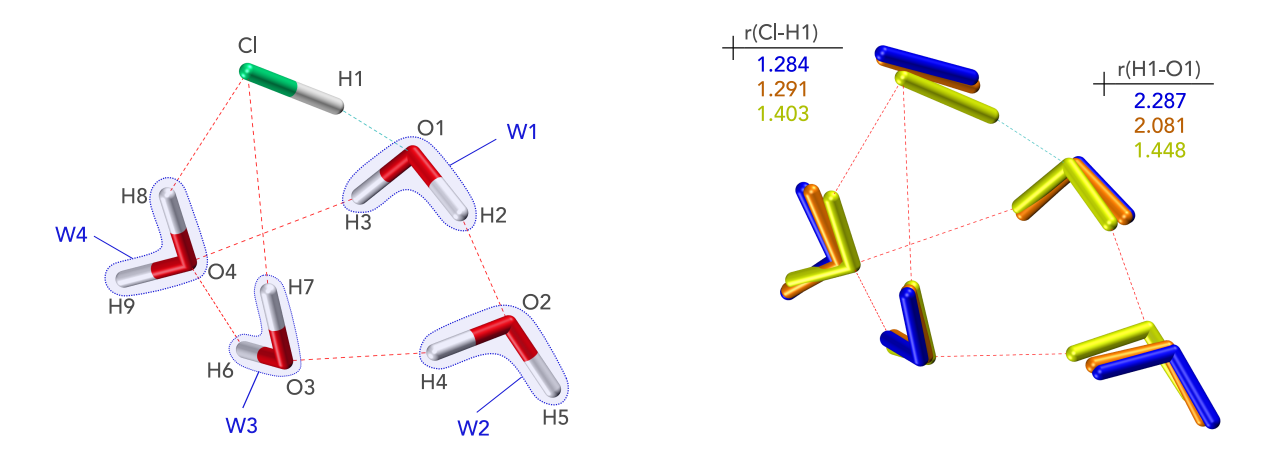


Figure 11: Left: structure of X_{18}^{4u} including atom labels used in the text. The blue labels refer to the individual water molecules. Right: Superposition of optimized geometries corresponding to the frozen (blue), polarized (orange) and fully relaxed (yellow) potential energy surface. The molecular geometries from adiabatic EDA are obtained using a $(HCl)(H_2O)_4$ reference. A significant HCl bond elongation occurs upon changing from the polarized to the fully relaxed PES.

angles associated with the minima on the frozen, polarized and fully relaxed PES are collected in Table 1. At the frozen level, the HCl bond length is virtually identical to r(HCl) in the gas phase. All OH-type hydrogen bonds at this level range between 2.22 Å and 2.37 Å, while the two Cl···H hydrogen bonds adopt values of ca. 3 Å. All seven H-bond angles are reduced compared to the ideal case, whereby \angle (O3-H6-O4) = 167° represents the largest and \angle (Cl-H8-O4) = 122° the smallest angle, respectively. As the fragments are allowed to polarize in the field of the other fragments, the cluster contracts with all hydrogen bonds shortening by 0.14 Å on average (see Fig. 11). Simultaneously, the Cl-H1 bond length undergoes a rather insignificant increase of 0.007 Å. The changes in H-bond angles are overall small, the largest of which being an increase of ca. 6° for \angle (Cl-H8-O4). Lifting the fragment constraint, i.e. transitioning from the polarized to the fully relaxed geometry entails the largest

structural changes. Most notably, the O1-H1 distance shortens significantly by 0.63 Å, while the Cl-H1 bond length extends by 0.11 Å. In order to accommodate the strong interaction of HCl and the acceptor water molecule (W1), i.e. the beginning charge separation of HCl into H⁺ and Cl⁻, all other hydrogen-bonds in the cluster undergo substantial shortening. Unsurprisingly, the largest reductions in hydrogen-bond length occur for fragment pairs involving HCl (Δr (Cl-H8) = -0.42 Å) or the acceptor water W1 (Δr (O2-H2) = -0.37 Å). Similarly, changes in H-bond length within the water ring structure are not equally large, but depend on the distance relative to the water molecule involved in the partial proton transfer (W1). The structural rearrangement at the fully relaxed level also manifest itself in the bond angles. The H-bond angles become more favorable overall with the exception of both O-H···O angles involving water W4, which decrease by 11° and 5°, respectively. The third H-bond angle involving W4 and HCl, \angle (Cl-H8-O4), on the other hand increases by 11°. W4 therefore adopts a slightly less favorable orientation within the water tetramer in order to strengthen the charge-transfer interaction (HCl \rightarrow W4).

The changes due to charge-transfer can be further analyzed by separating the overall charge-transfer into contributions from forward and backward donations using the variational forward-backward (VFB) scheme. ⁸⁹ In order to isolate the effect of charge-transfer between HCl and the water tetramer, the two-fragment reference (HCl)(($\rm H_2O)_4$) is employed for the VFB analysis. Selected distances and angles are collected in Table S1. Starting from the water tetramer and HCl fragments on the polarized surface, the relaxation with respect to forward-CT (HCl \rightarrow ($\rm H_2O)_4$) leads to a considerable reduction of the Cl-H8 distance by 0.22 Å, which is about 60% of the entire difference due to charge-transfer. The forward-CT has only a negligible effect on the HCl distance and other H-bonds. Allowing for backward-CT only (($\rm H_2O)_4 \rightarrow \rm HCl$) on the other hand, drastically shortens the O1-H1 distance by 0.44 Å (72% of CT difference) and simultaneously weakens the H1-Cl bond by 0.05 Å (48% of CT difference). Interestingly, backward-CT also leads to a noticeable reduction of r(H8-Cl) and r(H7-Cl) (18% and 44% of CT difference), which cannot be rationalized by a charge-

Table 1: Selected bond lengths (r) and angles (\measuredangle) of optimized \mathbf{X}_{18}^{4u} geometries corresponding to minima on the frozen (FRZ), polarized (POL) and fully relaxed potential energy surface (FULL) as well as their respective differences Δ_1 and Δ_2 . All interatomic distances are given in Å and bond angles are given in degree. The 5-fragment reference (HCl)(H₂O)₄ was employed in the adiabatic ALMO calculations.

	FRZ	Δ_1	POL	Δ_2	FULL
r(Cl-H1)	1.284	0.007	1.291	0.112	1.403
r(O1-H1)	2.287	-0.206	2.081	-0.633	1.448
r(Cl-H7)	3.070	-0.073	2.997	-0.290	2.708
r(Cl-H8)	3.009	-0.221	2.788	-0.415	2.373
r(O2-H2)	2.260	-0.154	2.106	-0.374	1.732
r(O3-H4)	2.217	-0.144	2.073	-0.274	1.799
r(O4-H6)	2.297	-0.135	2.162	-0.143	2.019
r(O4-H3)	2.374	-0.074	2.300	-0.137	2.163
∡(Cl-H1-O1)	157.5	2.9	160.3	10.4	170.8
∡(Cl-H7-O3)	127.8	-0.4	127.3	4.2	131.5
∠(Cl-H8-O4)	122.4	6.2	128.5	11.1	139.6
∡(O1-H2-O2)	156.0	-0.2	155.8	9.2	165.0
∠(O2-H4-O3)	158.8	2.2	161.0	0.4	161.4
∠(O3-H6-O4)	167.3	-0.1	167.2	-10.7	156.5
∠(O4-H3-O1)	141.1	-1.2	139.9	-5.1	134.8

transfer effects from HCl to $(H_2O)_4$. This H-bond shortening must therefore arise from a more favourable electrostatic interaction due to mutual polarization and charge-transfer within the water tetramer fragment $(H_2O)_4$.

Turning to the example of \mathbf{U}_{14}^{4u} , each fragment acts as a single H-bond donor and acceptor (in contrast to \mathbf{X}_{18}^{4u}). A selection of H-bond lengths and angles corresponding to the frozen, polarized and fully relaxed surface is provided in the supporting information (Table S2). At the frozen level the cluster still adopts a circular nearly planar configuration (see Fig. 12), but is expanded due to increased H-bond lengths. Similarly to \mathbf{X}_{18}^{4u} , the HCl bond length is virtually identical to its isolated gas-phase analogue. Moving to the polarized surface, the cluster contracts as H-bonds are shortened by 0.17 Å on average. There are, however, no noticeable changes to the hydrogen-bonding angles due to the symmetry of the geometric rearrangement. In agreement with the observations for \mathbf{X}_{18}^{4u} , allowing the mutual polarization

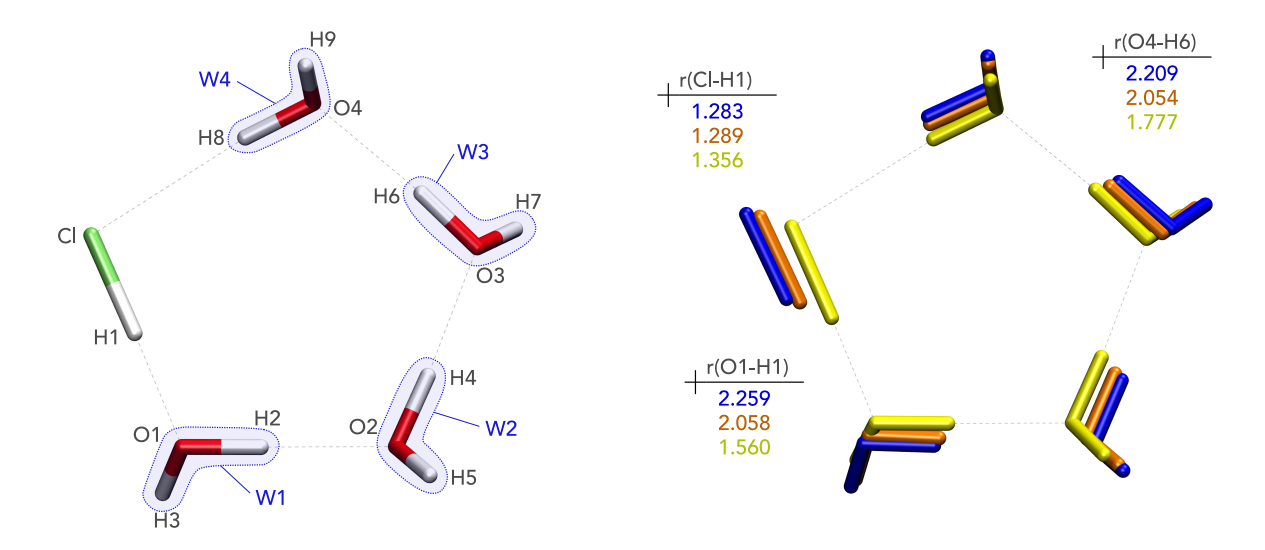


Figure 12: Left: structure of U_{14}^{4u} including atom labels used in the text. The blue labels refer to the individual water molecules. Right: Superposition of optimized geometries corresponding to the frozen (blue), polarized (orange) and fully relaxed (yellow) potential energy surface. The molecular geometries from adiabatic EDA are obtained using a $(HCl)(H_2O)_4$ reference. Lifting the ALMO constraints leads to a compression of the cluster geometry.

of fragments (without exchange of electron density) weakens the HCl bond only marginally $(\Delta r(\text{H1-Cl}) < 0.01\,\text{Å})$. Upon switching to the fully relaxed surface, the O1-H1 distance reduces by 0.5 Å, simultaneously inducing an elongation of the HCl bond by 0.07 Å. The remaining water molecules adapt to the strengthened HCl-W1 interaction by reducing all other H-bond distances (0.32 Å on average) further contracting the cluster geometry.

Another example is \mathbf{P}_{23}^{4u} belonging to the partial aggregate type, which has previously been identified to be a precursor species leading to the solvent-shared ion pair (\mathbf{S}_{1}^{4d}) dissociated cluster. ¹⁹ The H-accepting water W1 in this arrangement acts as a double H-donor, while HCl corresponds to a single H-acceptor thus limiting its capability to stabilize dissociation of HCl in comparison to \mathbf{X}_{18}^{4u} . Interestingly, the cluster adopts a completely different arrangement on the frozen surface, whereby the water tetramer forms a tetrahedron with the HCl hydrogen-bonded laterally (see Fig. 13 and Tab. S3). Allowing mutual polarization between fragments the cluster undergoes a larger rearrangement reverting back to the partial aggregate (\mathbf{P}) topology. Analogous to the previous examples, moving to the fully relaxed

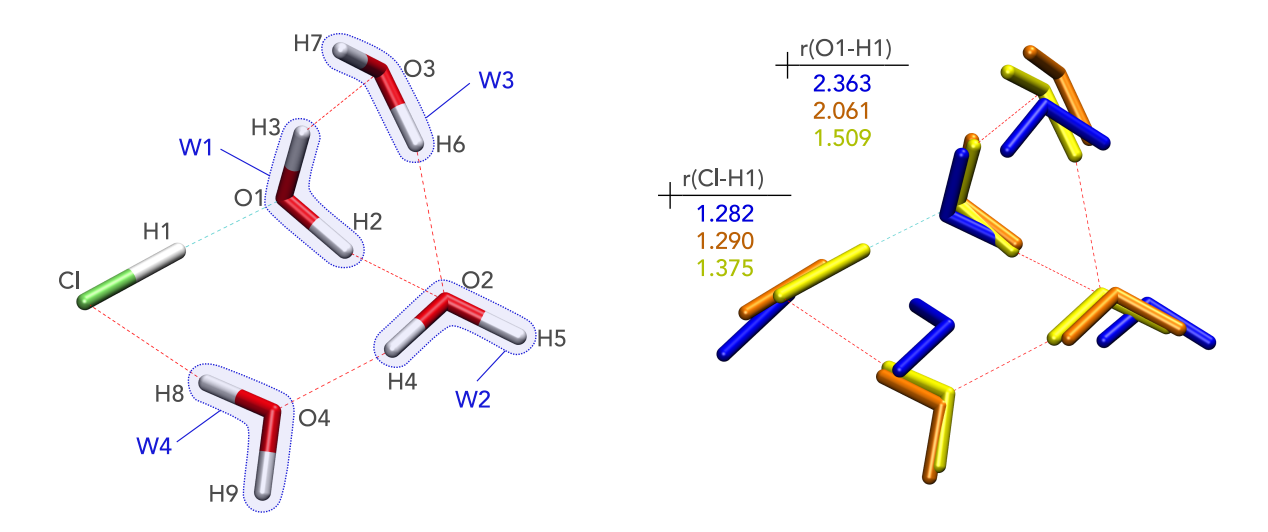


Figure 13: Left: structure of \mathbf{P}_{23}^{4u} including atom labels used in the text. The blue labels refer to the individual water molecules. Right: Superposition of optimized geometries corresponding to the frozen (blue), polarized (orange) and fully relaxed (yellow) potential energy surface. The molecular geometries from adiabatic EDA are obtained using a $(HCl)(H_2O)_4$ reference. In contrast to the polarized and fully relaxed surface, there is no minimum corresponding to the **P**-motif on the frozen surface.

surface entails a drastic shortening of the O1-H1 distance (-0.55 Å) and elongation of the HCl bond (0.08 Å). As the water network adapts to the strong W1-HCl interaction, the H-bond between W1 and W2 experiences the smallest shortening overall (-0.18 Å), whereas W3 reduces its H-bond distance to W1 by almost twice as much $(\Delta r(\text{O3-H3}) = -0.32 \text{ Å})$. The geometric effect associated with charge-transfer is less pronounced for W2 due to its double H-acceptor role, whereas W3 only couples to one hydrogen atom (H3).

The trend of the HCl bond length on the frozen, polarized, and fully relaxed PES is very similar for all 12 examples. As can be seen from Fig. 14 the HCl bond length becomes weakened as the ALMO constraints are lifted step-by-step. On the frozen and polarized surface the electric field exerted on HCl by the water molecules is not strong enough to induce a significant increase of the HCl bond length. We also notice that the obtained HCl distances on the frozen and polarized surface are consistent with respect to the chosen fragment reference. In other words, on either surface r(HCl) remains mostly unaffected whether the water molecules are treated as a single fragment or as individual fragments. Allowing

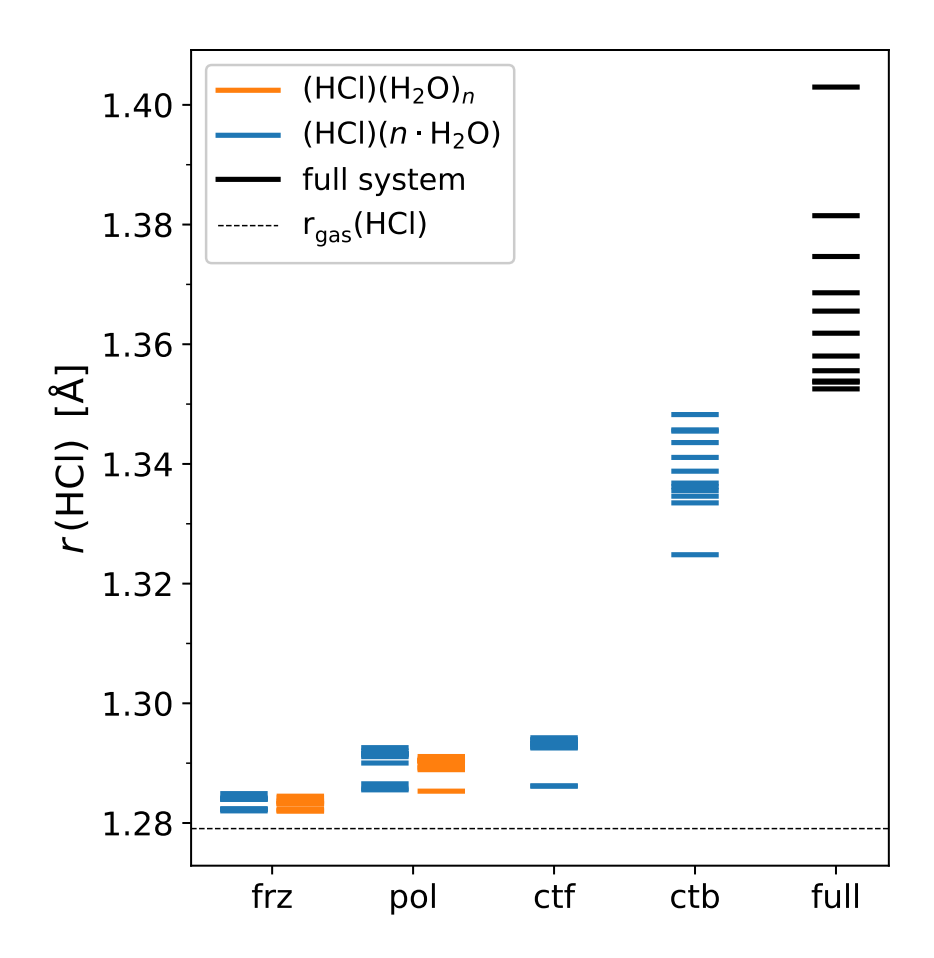


Figure 14: HCl bond lengths r(HCl) of selected $\text{HCl}(\text{H}_2\text{O})_n$ clusters (n=[3,4]) optimized corresponding to the frozen (frz), polarized (pol) and fully relaxed (full) wavefunction. Additionally, results allowing forward (ctf, $\text{HCl} \rightarrow (\text{H}_2\text{O})_4$) and backward charge-transfer (ctb, $\text{HCl} \leftarrow (\text{H}_2\text{O})_4$) are shown. The geometries from adiabatic EDA were obtained using two different undissociated references with either all water molecules as one fragment (blue) or as individual fragments (orange). The dotted line corresponds to the HCl bond length in the gas phase at $\omega \text{B97M-V/def2-TZVPD}$ level of theory $(r(\text{HCl}) = 1.279\,\text{Å})$. Destabilization of r(HCl) as observed in the supersystem does not follow from either forward-CT or backward-CT alone, but from the synergy of both.

the geometry to relax with respect to forward CT ($\mathrm{HCl} \rightarrow (\mathrm{H_2O})_4$) also does not lead to a noticeable destabilization of the HCl bond. The most prominent increase occurs moving to the backward CT ($\mathrm{HCl} \leftarrow (\mathrm{H_2O})_4$) surface, which is in accordance with the familiar mechanism of bond destabilization by interaction of lone pair and antibonding σ^* orbitals. It should be noted that the outliers on the forward CT or backward CT surface exhibiting a short HCl bond length are due to the structure collapsing onto a more weakly interacting cluster

geometry during the optimization (e.g. $U\rightarrow A$). The separation of forward and backward CT also shows that neither effect alone is sufficient to reach the extent of HCl bond elongation in these 12 examples. These weakened HCl bonds can only occur due to the synergy of population of the antibonding $\sigma^*(HCl)$ orbital (backward CT) and stabilization of the increasingly anionic chlorine atom (forward CT).

Conclusion

The present study set out to examine the effect of intermolecular forces for the dissociation of HCl in $(H_2O)_n$ nanoclusters up to n=4. For this purpose a set of 45 HCl-water clusters was considered. The r(HCl) bond length in the 35 undissociated clusters depends strongly on the geometry, whereby one neutral species (\mathbf{X}_{18}^{4u}) exhibits a particularly stretched HCl bond with $r(HCl)=1.406\,\text{Å}$. Two structural motifs were found to promote the HCl bond length elongation: (a) the primary water (H-bond acceptor to HCl) acts as double H-bond donor and (b) the chlorine atom serves as double H-bond acceptor. These two motifs are also present in the \mathbf{X}_4^{3u} cluster, which only contains three water molecules but involves a stretched HCl bond $(r(HCl)=1.381\,\text{Å})$ nonetheless. The dissociated form (\mathbf{X}_6^{3d}) of this cluster was also obtained, which represents the only example of a dissociated cluster with less than four water molecules in the present set. However, the existence of the corresponding PES minimum was shown to depend on the applied level of theory and should thus be interpreted with caution.

Intermolecular interactions arising in these HCl-water nanoclusters were studied using the vertical and adiabatic ALMO-EDA schemes. The vertical EDA scheme was applied to two proton-transfer PES coordinates (based on X_{18}^{4u} and P_{23}^{4u}), whereby the effect of the water network was probed by incrementally solvating $HCl \cdot H_2O$. The results show that a minimum of three water molecules is needed in order stabilize the dissociated species relative to the undissociated cluster, while four water molecules are necessary to achieve significant

relative stabilization of the dissociated species. Adiabatic EDA results of twelve nanoclusters with elongated HCl bond lengths showed no significant HCl bond stretching at the frozen or polarized level, thus establishing charge-transfer as the main contribution. Further decomposition of the charge-transfer term into forward- and backward-CT confirmed the well-known $n(O) \rightarrow \sigma^*(HCl)$ orbital interaction (here termed backward-CT) as the dominating component of the HCl bond destabilization. However, the backward-CT component alone is insufficient to achieve the full extent of HCl bond destabilization. Thus, the adiabatic EDA results suggest that a push-pull mechanism based on the synergy of forward-CT and backward-CT is needed in order to drive the HCl bond towards the brink of dissociation. A natural progression of this work is to extend the analysis presented herein to other hydrohalic acid - water nanoclusters and to examine the minimum number of water molecules required for dissociation, as well as the transferability of the push-pull driving force for dissociation.

Conflicts of Interest

The authors declare the following competing financial interest(s): M. Head-Gordon is a part-owner of Q-Chem Inc, whose software was used to perform the electronic structure calculations reported in this research.

Acknowledgement

We acknowledge support from the U.S. National Science Foundation through Grant No. CHE-1955643, and additional support from CALSOLV. A.Z. gratefully acknowledges financial support from the Swiss National Science Foundation through the Early Postdoc. Mobility fellowship.

References

- (1) Laasonen, K.; Klein, M. L. Ab Initio Molecular Dynamics Study of Hydrochloric Acid in Water. J. Am. Chem. Soc. 1994, 116, 11620–11621.
- (2) Sillanpää, A. J.; Simon, C.; Klein, M. L.; Laasonen, K. Structural and Spectral Properties of Aqueous Hydrogen Fluoride Studied Using ab Initio Molecular Dynamics. J. Phys. Chem. B 2002, 106, 11315–11322.
- (3) McGrath, M. J.; Kuo, I.-F. W.; Ngouana W., B. F.; Ghogomu, J. N.; Mundy, C. J.; Marenich, A. V.; Cramer, C. J.; Truhlar, D. G.; Siepmann, J. I. Calculation of the Gibbs free energy of solvation and dissociation of HCl in water via Monte Carlo simulations and continuum solvation models. *Phys. Chem. Chem. Phys.* 2013, 15, 13578–13578.
- (4) Baer, M. D.; Tobias, D. J.; Mundy, C. J. Investigation of Interfacial and Bulk Dissociation of HBr, HCl, and HNO3 Using Density Functional Theory-Based Molecular Dynamics Simulations. J. Phys. Chem. C 2014, 118, 29412–29420.
- (5) Kim, C. K.; Park, B. H.; Sohn, C. K.; Yu, Y. H.; Kim, C. K. Computational Study on Protolytic Dissociation of HCl and HF in Aqueous Solution. *Bull. Korean Chem. Soc.* 2014, 35, 1029–1035.
- (6) Rizzuto, A. M.; Cheng, E. S.; Lam, R. K.; Saykally, R. J. Surprising Effects of Hydrochloric Acid on the Water Evaporation Coefficient Observed by Raman Thermometry. J. Phys. Chem. C 2017, 121, 4420–4425.
- (7) Gertner, B. J.; Hynes, J. T. Molecular Dynamics Simulation of Hydrochloric Acid Ionization at the Surface of Stratospheric Ice. *Science* **1996**, *271*, 1563–1566.
- (8) Svanberg, M.; Pettersson, J. B. C.; Bolton, K. Coupled QM/MM molecular dynamics simulations of HCl interacting with ice surfaces and water clusters evidence of rapid ionization. J. Phys. Chem. A 2000, 104, 5787–5798.

- (9) Bolton, K.; Pettersson, J. B. C. Ice-Catalyzed Ionization of Hydrochloric Acid. *J. Am. Chem. Soc.* **2001**, *123*, 7360–7363.
- (10) Al-Halabi, A.; Bianco, R.; Hynes, J. T. Acid Dissociation of HBr on a Model Ice Surface.
 J. Phys. Chem. A 2002, 106, 7639–7645.
- (11) Devlin, J. P.; Uras, N.; Sadlej, J.; Buch, V. Discrete stages in the solvation and ionization of hydrogen chloride adsorbed on ice particles. *Nature* **2002**, *417*, 269–271.
- (12) Parent, P.; Laffon, C. Adsorption of HCl on the Water Ice Surface Studied by X-ray Absorption Spectroscopy. J. Phys. Chem. B 2005, 109, 1547–1553.
- (13) Parent, P.; Lasne, J.; Marcotte, G.; Laffon, C. HCl adsorption on ice at low temperature: a combined X-ray absorption, photoemission and infrared study. *Phys. Chem. Chem. Phys.* **2011**, *13*, 7142–7148.
- (14) Packer, M. J.; Clary, D. C. Interaction of HCl with water clusters: $(H_2O)_nHCl$, n = 1-3. J. Phys. Chem. 1995, 99, 14323–14333.
- (15) Planas, M.; Lee, C.; Novoa, J. J. Kinetics of the Proton Transfer in X··· (H2O)4 Clusters (X = H₂O, NH₃, H₂S, and HCl): Evidence of a Concerted Mechanism. J. Phys. Chem. 1996, 100, 16495–16501.
- (16) Conley, C.; Tao, F.-M. Ionic dissociation of hydrogen bromide in water clusters: a computational study. *Chem. Phys. Lett.* **1999**, *301*, 29–36.
- (17) Smith, A.; Vincent, M. A.; Hillier, I. H. Mechanism of Acid Dissociation in Water Clusters: Electronic Structure Studies of (H2O)_nHX (n = 4, 7; X = OH, F, HS, HSO₃, OOSO₂H, OOH·SO₂). J. Phys. Chem. A 1999, 103, 1132–1139.
- (18) Kuo, J.-L.; Klein, M. L. Dissociation of hydrogen fluoride in HF(H(2)O)(7). *J. Chem. Phys.* **2004**, *120*, 4690–4695.

- (19) Forbert, H.; Masia, M.; Kaczmarek-Kedziera, A.; Nair, N. N.; Marx, D. Aggregation-Induced Chemical Reactions: Acid Dissociation in Growing Water Clusters. J. Am. Chem. Soc. 2011, 133, 4062–4072.
- (20) Letzner, M.; Gruen, S.; Habig, D.; Hanke, K.; Endres, T.; Nieto, P.; Schwaab, G.; Walewski, Ł.; Wollenhaupt, M.; Forbert, H.; Marx, D.; Havenith, M. High resolution spectroscopy of HCl-water clusters: IR bands of undissociated and dissociated clusters revisited. J. Chem. Phys. 2013, 139, 154304–154304.
- (21) Mani, D.; de Tudela, R. P.; Schwan, R.; Pal, N.; Körning, S.; Forbert, H.; Redlich, B.; van der Meer, A. F. G.; Schwaab, G.; Marx, D.; Havenith, M. Acid solvation versus dissociation at "stardust conditions": Reaction sequence matters. Sci. Adv. 2019, 5, eaav8179–eaav8179.
- (22) Solomon, S.; Garcia, R. R.; Rowland, F. S.; Wuebbles, D. J. On the depletion of Antarctic ozone. *Nature* **1986**, *321*, 755–758.
- (23) Molina, M. J.; Tso, T.-L.; Molina, L. T.; Wang, F. C.-Y. Antarctic Stratospheric Chemistry of Chlorine Nitrate, Hydrogen Chloride, and Ice: Release of Active Chlorine. Science 1987, 238, 1253–1257.
- (24) Shevkunov, S. V. Can Water Clusters Ionize HCl under the Conditions of Arctic Stratosphere? 1. Intermolecular Interactions. *Colloid J.* **2004**, *66*, 216–229.
- (25) Huthwelker, T.; Ammann, M.; Peter, T. The Uptake of Acidic Gases on Ice. Chem. Rev. 2006, 106, 1375–1444.
- (26) Turco, R. P.; Toon, O. B.; Hamill, P. Heterogeneous physicochemistry of the polar ozone hole. *J. Geophys. Res.* **1989**, *94*, 16493–16493.
- (27) Kang, H.; Shin, T.-H.; Park, S.-C.; Kim, I. K.; Han, S.-J. Acidity of Hydrogen Chloride on Ice. J. Am. Chem. Soc. **2000**, 122, 9842–9843.

- (28) Gutberlet, A.; Schwaab, G.; Birer, O.; Masia, M.; Kaczmarek, A.; Forbert, H.; Havenith, M.; Marx, D. Aggregation-Induced Dissociation of HCl(H2O)4 Below 1 K: The Smallest Droplet of Acid. *Science* **2009**, *324*, 1545–1548.
- (29) Re, S.; Osamura, Y.; Suzuki, Y.; Schaefer, H. F. Structures and stability of hydrated clusters of hydrogen chloride, HCl(H2O)n, n=1–5. *J. Chem. Phys.* **1998**, *109*, 973–977.
- (30) Cabaleiro-Lago, E. M.; Hermida-Ramón, J. M.; Rodríguez-Otero, J. Computational study of the dissociation of H–X acids (X=F, Cl, Br, I) in water clusters. *J. Chem. Phys.* **2002**, *117*, 3160–3168.
- (31) Odde, S.; Mhin, B. J.; Lee, S.; Lee, H. M.; Kim, K. S. Dissociation chemistry of hydrogen halides in water. *J. Chem. Phys.* **2004**, *120*, 9524–9535.
- (32) Vargas-Caamal, A.; Cabellos, J. L.; Ortiz-Chi, F.; Rzepa, H. S.; Restrepo, A.; Merino, G. How Many Water Molecules Does it Take to Dissociate HCl? *Chem. Eur. J* **2016**, *22*, 2812–2818.
- (33) Milet, A.; Struniewicz, C.; Moszynski, R.; Wormer, P. E. S. Theoretical study of the protolytic dissociation of HCl in water clusters. *J. Chem. Phys.* **2001**, *115*, 349–356.
- (34) Boda, M.; Naresh Patwari, G. Insights into acid dissociation of HCl and HBr with internal electric fields. *Phys. Chem. Chem. Phys.* **2017**, *19*, 7461–7464.
- (35) Stone, A. J. The Theory of Intermolecular Forces; Oxford University Press, 2013.
- (36) Kitaura, K.; Morokuma, K. A new energy decomposition scheme for molecular interactions within the Hartree-Fock approximation. *Int. J. Quantum Chem.* **1976**, *10*, 325–340.
- (37) Ziegler, T.; Rauk, A. On the calculation of bonding energies by the Hartree Fock Slater method. *Theor. Chim. Acta* **1977**, 46, 1–10.

- (38) Bagus, P. S.; Hermann, K.; Bauschlicher, C. W. A new analysis of charge transfer and polarization for ligand–metal bonding: Model studies of Al4CO and Al4NH3. *J. Chem. Phys.* **1984**, *80*, 4378–4386.
- (39) Glendening, E. D.; Streitwieser, A. Natural energy decomposition analysis: An energy partitioning procedure for molecular interactions with application to weak hydrogen bonding, strong ionic, and moderate donor–acceptor interactions. *J. Chem. Phys.* **1994**, 100, 2900–2909.
- (40) Jeziorski, B.; Moszynski, R.; Szalewicz, K. Perturbation Theory Approach to Intermolecular Potential Energy Surfaces of van der Waals Complexes. Chem. Rev. 1994, 94, 1887–1930.
- (41) Mo, Y.; Gao, J.; Peyerimhoff, S. D. Energy decomposition analysis of intermolecular interactions using a block-localized wave function approach. J. Chem. Phys. 2000, 112, 5530–5538.
- (42) Bickelhaupt, F. M.; Baerends, E. J. Reviews in Computational Chemistry; John Wiley & Sons, Inc.: Hoboken, NJ, USA, 2007; pp 1–86.
- (43) Khaliullin, R. Z.; Cobar, E. A.; Lochan, R. C.; Bell, A. T.; Head-Gordon, M. Unravelling the origin of intermolecular interactions using absolutely localized molecular orbitals. J. Phys. Chem. A 2007, 111, 8753–8765.
- (44) Mitoraj, M. P.; Michalak, A.; Ziegler, T. A Combined Charge and Energy Decomposition Scheme for Bond Analysis. *J. Chem. Theory Comput.* **2009**, *5*, 962–975.
- (45) Su, P.; Li, H. Energy decomposition analysis of covalent bonds and intermolecular interactions. *J. Chem. Phys.* **2009**, *131*, 014102.
- (46) Wu, Q.; Ayers, P. W.; Zhang, Y. Density-based energy decomposition analysis for

- intermolecular interactions with variationally determined intermediate state energies. J. Chem. Phys. **2009**, 131, 164112.
- (47) Schneider, W. B.; Bistoni, G.; Sparta, M.; Saitow, M.; Riplinger, C.; Auer, A. A.; Neese, F. Decomposition of Intermolecular Interaction Energies within the Local Pair Natural Orbital Coupled Cluster Framework. J. Chem. Theory Comput. 2016, 12, 4778–4792.
- (48) Szalewicz, K. Symmetry-adapted perturbation theory of intermolecular forces. Wiley Interdiscip. Rev.: Comput. Mol. Sci. 2012, 2, 254–272.
- (49) Parker, T. M.; Burns, L. A.; Parrish, R. M.; Ryno, A. G.; Sherrill, C. D. Levels of symmetry adapted perturbation theory (SAPT). I. Efficiency and performance for interaction energies. J. Chem. Phys. 2014, 140, 094106.
- (50) Arillo Flores, O. I.; Bernal-Uruchurtu, M. I. Charge separation process in water clusters containing HCl. Molecular dynamics study using semiempirical hamiltonians. *J. Phys. Chem. A* **2010**, *114*, 8975–8983.
- (51) Mackie, C.; Zech, A.; Head-Gordon, M. Effective Two-Body Interactions. J. Phys. Chem. A 2021, 125, 7750–7758.
- (52) Horn, P. R.; Sundstrom, E. J.; Baker, T. A.; Head-Gordon, M. Unrestricted absolutely localized molecular orbitals for energy decomposition analysis: theory and applications to intermolecular interactions involving radicals. *J. Chem. Phys.* **2013**, *138*, 134119.
- (53) Horn, P. R.; Mao, Y.; Head-Gordon, M. Probing non-covalent interactions with a second generation energy decomposition analysis using absolutely localized molecular orbitals. *Phys. Chem. Chem. Phys.* 2016, 18, 23067–23079.
- (54) Khaliullin, R. Z.; Bell, A. T.; Head-Gordon, M. Analysis of charge transfer effects in

- molecular complexes based on absolutely localized molecular orbitals. *J. Chem. Phys.* **2008**, *128*, 184112.
- (55) Horn, P. R.; Mao, Y.; Head-Gordon, M. Defining the contributions of permanent electrostatics, Pauli repulsion, and dispersion in density functional theory calculations of intermolecular interaction energies. J. Chem. Phys. 2016, 144, 114107.
- (56) Mao, Y.; Loipersberger, M.; Horn, P. R.; Das, A.; Demerdash, O.; Levine, D. S.; Prasad Veccham, S.; Head-Gordon, T.; Head-Gordon, M. From Intermolecular Interaction Energies and Observable Shifts to Component Contributions and Back Again: A Tale of Variational Energy Decomposition Analysis. *Annu. Rev. Phys. Chem.* 2021, 72, 641–666.
- (57) Horn, P. R.; Head-Gordon, M. Polarization contributions to intermolecular interactions revisited with fragment electric-field response functions. J. Chem. Phys. 2015, 143, 114111.
- (58) Mao, Y.; Horn, P. R.; Head-Gordon, M. Energy decomposition analysis in an adiabatic picture. *Phys. Chem. Chem. Phys.* **2017**, *19*, 5944–5958.
- (59) Mao, Y.; Ge, Q.; Horn, P. R.; Head-Gordon, M. On the Computational Characterization of Charge-Transfer Effects in Noncovalently Bound Molecular Complexes. J. Chem. Theory Comput. 2018, 14, 2401–2417.
- (60) Mao, Y.; Head-Gordon, M. Probing blue-shifting hydrogen bonds with adiabatic energy decomposition analysis. *J. Phys. Chem. Lett.* **2019**, *10*, 3899–3905.
- (61) Epifanovsky, E. et al. Software for the frontiers of quantum chemistry: An overview of developments in the Q-Chem 5 package. *J. Chem. Phys.* **2021**, *155*, 084801.
- (62) Weigend, F.; Ahlrichs, R. Balanced basis sets of split valence, triple zeta valence and

- quadruple zeta valence quality for H to Rn: Design and assessment of accuracy. *Phys. Chem. Chem. Phys.* **2005**, *7*, 3297–3305.
- (63) Rappoport, D.; Furche, F. Property-optimized gaussian basis sets for molecular response calculations. *J. Chem. Phys.* **2010**, *133*, 134105.
- (64) Mardirossian, N.; Head-Gordon, M. ωB97M-V: A combinatorially optimized, range-separated hybrid, meta-GGA density functional with VV10 nonlocal correlation.
 J. Chem. Phys. 2016, 144, 214110.
- (65) Mardirossian, N.; Head-Gordon, M. Thirty years of density functional theory in computational chemistry: an overview and extensive assessment of 200 density functionals. Mol. Phys. 2017, 115, 2315–2372.
- (66) Dasgupta, S.; Herbert, J. M. Standard grids for high-precision integration of modern density functionals: SG-2 and SG-3. *J. Comput. Chem.* **2017**, *38*, 869–882.
- (67) Gill, P. M. W.; Johnson, B. G.; Pople, J. A. A standard grid for density functional calculations. *Chem. Phys. Lett.* **1993**, *209*, 506–512.
- (68) Becke, A. D. Density-functional exchange-energy approximation with correct asymptotic behavior. *Phys. Rev. A* **1988**, *38*, 3098–3100.
- (69) Lee, C.; Yang, W.; Parr, R. G. Development of the Colle-Salvetti correlation-energy formula into a functional of the electron density. *Phys. Rev. B* **1988**, *37*, 785–789.
- (70) Sherrill, C. D.; Lee, M. S.; Head-Gordon, M. On the performance of density functional theory for symmetry-breaking problems. *Chem. Phys. Lett.* **1999**, *302*, 425–430.
- (71) Stephens, P. J.; Devlin, F. J.; Chabalowski, C. F.; Frisch, M. J. Ab Initio Calculation of Vibrational Absorption and Circular Dichroism Spectra Using Density Functional Force Fields. J. Phys. Chem. 1994, 98, 11623–11627.

- (72) Yanai, T.; Tew, D. P.; Handy, N. C. A new hybrid exchange–correlation functional using the Coulomb-attenuating method (CAM-B3LYP). *Chem. Phys. Lett.* **2004**, *393*, 51–57.
- (73) Becke, A. D. Density-functional thermochemistry. III. The role of exact exchange.

 J. Chem. Phys. 1993, 98, 5648–5652.
- (74) Weigend, F.; Köhn, A.; Hättig, C. Efficient use of the correlation consistent basis sets in resolution of the identity MP2 calculations. *J. Chem. Phys.* **2002**, *116*, 3175–3183.
- (75) Bannwarth, C.; Ehlert, S.; Grimme, S. GFN2-xTB-An Accurate and Broadly Parametrized Self-Consistent Tight-Binding Quantum Chemical Method with Multipole Electrostatics and Density-Dependent Dispersion Contributions. J. Chem. Theory Comput. 2019, 15, 1652–1671.
- (76) Pracht, P.; Bohle, F.; Grimme, S. Automated exploration of the low-energy chemical space with fast quantum chemical methods. *Phys. Chem. Chem. Phys.* **2020**, *22*, 7169–7192.
- (77) Arillo-Flores, O. I.; Ruiz-López, M. F.; Bernal-Uruchurtu, M. I. Can semi-empirical models describe HCl dissociation in water? *Theor. Chem. Acc.* **2007**, *118*, 425–435.
- (78) Wicke, E.; Eigen, M.; Ackermann, T. Über den Zustand des Protons (Hydroniumions) in wäßriger Lösung. Z. Phys. Chem. 1954, 1, 340–364.
- (79) Eigen, M. Protonenübertragung, Säure-Base-Katalyse und enzymatische Hydrolyse. Teil I: Elementarvorgänge. *Angew. Chem.* **1963**, *75*, 489–508.
- (80) Eigen, M. Proton transfer, acid-base catalysis, and enzymatic hydrolysis. Part I: elementary processes. *Angew. Chem. Int. Ed. Engl.* **1964**, *3*, 1–19.
- (81) Bacelo, D. E.; Binning, R. C.; Ishikawa, Y. Ab Initio Monte Carlo Simulated Annealing Study of HCl(H2O)n (n = 3, 4) Clusters. *J. Phys. Chem. A* **1999**, *103*, 4631–4640.

- (82) Limbach, H.-H.; Tolstoy, P. M.; Pérez-Hernández, N.; Guo, J.; Shenderovich, I. G.; Denisov, G. S. OHO Hydrogen Bond Geometries and NMR Chemical Shifts: From Equilibrium Structures to Geometric H/D Isotope Effects, with Applications for Water, Protonated Water, and Compressed Ice. Isr. J. Chem. 2009, 49, 199–216.
- (83) Gonzalez, J. D.; Florez, E.; Romero, J.; Reyes, A.; Restrepo, A. Microsolvation of Mg2+, Ca2+: strong influence of formal charges in hydrogen bond networks. J. Mol. Model. 2013, 19, 1763–1777.
- (84) Herbert, J. M.; Carter-Fenk, K. Electrostatics, Charge Transfer, and the Nature of the Halide–Water Hydrogen Bond. J. Phys. Chem. A 2021, 125, 1243–1256.
- (85) Amirand, C.; Maillard, D. Spectrum and structure of water-rich water—hydracid complexes from matrix isolation spectroscopy: evidence for proton transfer. J. Mol. Struct. 1988, 176, 181–201.
- (86) Sobolewski, A. L.; Domcke, W. Photochemistry of HCl(H2O)4: Cluster Model of the Photodetachment of the Chloride Anion in Water. J. Phys. Chem. A 2003, 107, 1557– 1562.
- (87) Walewski, L.; Forbert, H.; Marx, D. Quantum Induced Bond Centering in Microsolvated HCl: Solvent Separated versus Contact Ion Pairs. J. Phys. Chem. Lett. **2011**, 2, 3069–3074.
- (88) Bresnahan, C. G.; David, R.; Milet, A.; Kumar, R. Ion Pairing in HCl-Water Clusters: From Electronic Structure Investigations to Multiconfigurational Force-Field Development. J. Phys. Chem. A 2019, 123, 9371–9381.
- (89) Loipersberger, M.; Mao, Y.; Head-Gordon, M. Variational Forward-Backward Charge Transfer Analysis Based on Absolutely Localized Molecular Orbitals: Energetics and Molecular Properties. J. Chem. Theory Comput. 2020, 16, 1073–1089.